

# Turbulent Flow over Steep Steady and Unsteady Waves under Strong Wind Forcing

PETER P. SULLIVAN

*National Center for Atmospheric Research, Boulder, Colorado*

MICHAEL L. BANNER AND RUSSEL P. MORISON

*School of Mathematics and Statistics, University of New South Wales, Sydney, New South Wales, Australia*

WILLIAM L. PEIRSON

*New College, University of New South Wales, Sydney, New South Wales, Australia*

(Manuscript received 15 June 2017, in final form 10 October 2017)

## ABSTRACT

Turbulent flow over strongly forced steep steady and unsteady waves is simulated using large-eddy simulation (LES) with time  $t$  and space  $\mathbf{x}$  varying wave height  $h(\mathbf{x}, t)$  imposed as a lower boundary condition. With steady waves,  $h(\mathbf{x}, t)$  is based on measurements of incipient and active breaking waves collected in a wind-wave flume, while a numerical wave code is used to generate an unsteady evolving wave packet (group). Highly intermittent airflow separation is found in the simulations, and the results suggest separation near a wave crest occurs prior to the onset of wave breaking. The form (pressure) drag is most sensitive to the wave slope, and the form drag can contribute as much as 74% to the total stress. Wind and scalar profiles from the LES display log-linear variations above the wave surface; the LES wind profiles are in good agreement with the measurements. The momentum roughness increases as the water surface changes from wind ripples to incipient breaking to active breaking. However, the scalar roughness decreases as the wave surface becomes rougher. This highlights major differences in momentum and scalar transport over a rough wavy surface. For a rapidly evolving, strongly forced wave group, the form drag is highly correlated with the wave slope, and intermittent separation is found early in the packet evolution when the local wave slope  $-\partial h/\partial x(\mathbf{x}, t) \geq 0.22$ . The packet root-mean-square wave slope is 0.084, but the form drag fraction is 2.4 times larger than a comparably forced steady wave. Thus, a passing wave group can induce unsteadiness in the wind stress.

## 1. Introduction

Turbulent flow over steep ocean surface waves is one of the key couplings in air–sea interaction. Steep waves are temporally and spatially transient disturbances characterized by airflow separation and wave breaking. The latter processes are especially important as they alter the equilibrium stress partitioning between form (pressure) and viscous drag and thus induce unsteadiness in the wind stress. Episodic breaking waves across a range of scales are also a stochastic source of momentum and energy for the underlying currents (Sullivan et al. 2007; Perlin et al. 2013). Intermittent airflow dynamics over steep breaking waves also plays a central role in numerous application areas, for example, setting the values of the surface exchange coefficients

for momentum and scalars ( $C_D$ ,  $C_K$ ) at high winds (Donelan et al. 2004; Black et al. 2007), controlling air–sea gas transfer (Wanninkhof et al. 2009), production of aerosols (Hwang et al. 2016), and altering microwave signatures (Banner and Fooks 1985; Melville et al. 1988).

Because of intrinsic nonlinearities, the present understanding of the details of airflow separation over steep waves and its connection to wave breaking is far from complete. Past modeling of wind–wave interaction has focused on linear regimes with steady waves of low wave slope (no separation) using Reynolds-averaged closures [see review by Belcher and Hunt (1998)] and ignores the presence of wave groups. The recent analytic work by Sajjadi et al. (2014, 2016) and Drullion and Sajjadi (2016) are exceptions, as their analysis emphasizes the importance of a time-dependent multimode wave field. Banner and Melville (1976) developed an analytic criterion for separation that hinges on the

*Corresponding author:* Peter P. Sullivan, pps@ucar.edu

DOI: 10.1175/JPO-D-17-0118.1

© 2018 American Meteorological Society. For information regarding reuse of this content and general copyright information, consult the [AMS Copyright Policy \(www.ametsoc.org/PUBSReuseLicenses\)](https://www.ametsoc.org/PUBSReuseLicenses).

presence of wave breaking but does not account for turbulent fluctuations and unsteadiness of the boundary (Miron and Vétel 2015). Recently, Veron et al. (2007), Reul et al. (2008), Buckley (2015), and Buckley and Veron (2016) stimulated further interest in flow over steep waves as they are able to identify intermittent air-flow separation using particle image velocimetry (PIV) techniques in laboratory wind-wave experiments under conditions where wave breaking is often weak or absent. Carefully designed laboratory measurements by Peirson and Garcia (2008), Grare et al. (2013b), and Peirson et al. (2014) also quantify the role of wave steepness [or wave slope  $ak$ , where  $(a, k)$  are the wave amplitude and wave-number, respectively] on form drag and wave growth. Turbulence-resolving direct numerical simulation (DNS) and large-eddy simulation (LES) provide additional insights into the interaction between turbulence and waves, but past studies tend to concentrate on canonical steady wave regimes of modest wave slope  $0.1 < ak < 0.25$  (e.g., Sullivan et al. 2000; Yang and Shen 2010; Sullivan et al. 2014a; Hara and Sullivan 2015; Druzhinin et al. 2016; Yang and Shen 2017). In this context, the present study contributes new insights regarding the role of breaking in the onset of airflow separation and the significance of the modulational structure of the waves in determining the form drag and wind stress.

The present work adopts a high Reynolds number LES perspective. We simulate turbulent flow over steep, strongly forced waves as observed in a wind-wave flume but sidestep the complexity of a fully coupled air–water interface. We adopt a view that important aspects of the problem can be gleaned by simulating the turbulent airflow with imposed surface waves, that is, by externally imposing the time  $t$  and space  $\mathbf{x}$  varying wave height  $h(\mathbf{x}, t)$ . This approach is then similar to the large body of previous work for flow over linear waves, but ours is unconventional in that we use observed and simulated fields of  $h(\mathbf{x}, t)$  as a lower boundary condition in the LES; thus, the imposed steep wave trains are physically realizable and not monochromatic. We are particularly interested in the roles of flow separation and wave steepness in setting the drag of the water surface and how airflow separation modifies passive scalar exchange. Both steady and unsteady wave trains are examined. The outline of the manuscript is as follows: Section 2 briefly introduces the governing equations and LES model and also shows how an ensemble closure can be developed from the LES equations. Section 3 describes the simulation details. Results for steep steady and unsteady wave trains are discussed in sections 4 and 5, respectively. A summary of the major findings are outlined in section 6. The appendix describes the details of how our unsteady wave packet is constructed.

## 2. Governing equations

### a. LES model

Our LES code for the marine atmospheric boundary layer above a spectrum of moving waves (Sullivan et al. 2014a) serves as the template for modeling turbulent flow over waves generated in a wind-wave flume. To adapt this LES model to the present application we eliminate system rotation and stratification, shrink the size of the computational domain to focus on the wave boundary layer, and impose measured and simulated wave fields as surface boundary conditions. The simulation details are described in section 3a.

We provide a brief overview of the LES model and solution algorithm in order to introduce the coordinate system and variables used in the simulations [see also Sullivan et al. (2014a)]. The following notation is used:  $\mathbf{u} \equiv (u, v, w)$  denotes the Cartesian velocity components,  $b$  is a passive scalar, and  $p$  is the pressure variable normalized by density  $\rho$ . The three Cartesian coordinates are  $\mathbf{x} \equiv x_i \equiv (x, y, z)$ , which are also referred to as streamwise, spanwise, and vertical directions, respectively. Flow variables  $(u_i, b, p)$  are interpreted as LES spatially filtered quantities. The set of spatially filtered LES equations that describe incompressible turbulent flow in a channel with a flat upper boundary are

$$\frac{\partial u_i}{\partial x_i} = 0, \quad (1a)$$

$$\frac{\partial u_i}{\partial t} = -\frac{\partial u_j u_i}{\partial x_j} - \frac{\partial p}{\partial x_i} - \frac{\partial \tau_{ij}}{\partial x_j} - \frac{\partial \mathcal{P}}{\partial x_i} \delta_{il}, \quad \text{and} \quad (1b)$$

$$\frac{\partial b}{\partial t} = -\frac{\partial u_i b}{\partial x_i} - \frac{\partial \tau_{ib}}{\partial x_i}. \quad (1c)$$

In the present application, the boundary layer winds are driven by a large-scale imposed external streamwise pressure gradient  $\partial \mathcal{P} / \partial x$  that is constant in space and time. To enforce mass conservation the pressure variable  $p$  is determined from an elliptic Poisson pressure equation  $\nabla^2 p = \mathcal{R}$  formed by applying the discrete divergence operator to the velocity time tendencies  $\nabla \cdot (\partial \mathbf{u})$ . To close the system of equations the subgrid-scale (SGS) momentum and scalar fluxes  $(\tau_{ij}, \tau_{ib})$ , respectively, require modeling in the interior of the flow and at the lower boundary. Many prescriptions have been proposed, and here we simply adopt well-tested eddy viscosity prescriptions  $(\nu_i, \nu_b) \sim \sqrt{e}$ , where  $e$  is the subgrid-scale kinetic energy. To compute eddy viscosity, we include an additional transport equation for SGS energy  $e$  in the LES equation set [(1)]. This prognostic equation for  $e$  includes a standard suite of terms,

namely, advection, production/destruction by shear and buoyancy, diffusion, and viscous dissipation. The molecular Reynolds number is assumed to be high and molecular diffusion terms are neglected. The specific formulas for the SGS fluxes used in our LES implementation are not repeated here but are documented in numerous references (see [Deardorff 1972](#); [Moeng 1984](#); [Moeng and Wyngaard 1989](#); [Sullivan et al. 1996](#); [McWilliams et al. 1999](#); [Sullivan et al. 2014a](#); [Moeng and Sullivan 2015](#)).

### b. LES equations in wave-following coordinates

The LES code integrates the governing equations in a time-varying, nonorthogonal, surface-following coordinate system. The computational coordinates are  $\xi_i = (\xi, \eta, \zeta)$ , and the wave-following grid transformation and metrics that map physical space to computational space  $(x, y, z, t) \Leftrightarrow (\xi, \eta, \zeta, t)$  are

$$\begin{aligned} x = \xi, \quad y = \eta, \quad z = \zeta + h(x, t) \left(1 - \frac{\zeta}{H}\right)^\varpi, \quad \text{and} \\ \xi_x = 1, \quad \zeta_x = -z_\xi J, \quad \zeta_z = 1/z_\zeta = J, \quad z_t = -\zeta_t/J, \end{aligned} \quad (2)$$

where  $h(x, t)$  is the time-varying surface wave height, and  $H$  is the top of the computational domain. The Jacobian of the mapping transformation  $J = \partial\zeta/\partial z$ , and the vertical coordinate lines move up and down with grid speed  $z_t \equiv \partial z/\partial t = -\partial\zeta/\partial t(1/J)$ . The slope of a wave-following streamwise gridline is  $z_\xi \equiv \partial z/\partial \xi = -\partial\zeta/\partial x(1/J)$ . Parameter  $\varpi$  controls how rapidly the streamwise gridlines become level surfaces with increasing distance from the surface in physical space, and we set  $\varpi = 3$  ([Sullivan et al. 2014a](#)). The transformation (2) is a smooth single-valued function and produces continuous spatial derivatives  $\partial\xi_i/\partial x_j$  and time derivatives  $\partial\xi_i/\partial t$ . The mapping allows an arbitrary shape to be imposed at the lower boundary with the gridlines translating vertically so as to follow the moving wave. The computational stencil uses collocated cell centered variables in combination with volume flux or “contravariant flux” velocities. Momentum and scalar advection are compactly written in strong flux-conservation form using the contravariant flux velocity

$$U_i = \frac{u_j}{J} \frac{\partial \xi_j}{\partial x_i}, \quad (3)$$

positioned at cell faces;  $U_i = (U, V, W)$  are normal to a surface of constant  $\xi_i$ . The use of contravariant flux velocities mimics the tight velocity–pressure coupling that is achieved in codes with a staggered layout of velocity and pressure variables.

In surface-fitted wave-following coordinates the LES equation set is

$$\frac{\partial U_i}{\partial \xi_i} = 0, \quad (4a)$$

$$\frac{\partial}{\partial t} \left( \frac{1}{J} \right) - \frac{\partial z_t}{\partial \zeta} = 0, \quad (4b)$$

$$\begin{aligned} \frac{\partial}{\partial t} \left( \frac{u_i}{J} \right) + \frac{\partial}{\partial \xi_j} [(U_j - \delta_{3j} z_t) u_i] = - \frac{\partial}{\partial \xi_j} \left( \frac{p}{J} \frac{\partial \xi_j}{\partial x_i} \right) \\ - \frac{\partial}{\partial \xi_j} \left( \frac{\tau_{ik}}{J} \frac{\partial \xi_j}{\partial x_k} \right) - \frac{1}{J} \frac{\partial \mathcal{P}}{\partial x_i} \delta_{il}, \end{aligned} \quad (4c)$$

$$\frac{\partial}{\partial t} \left( \frac{b}{J} \right) + \frac{\partial}{\partial \xi_j} [(U_j - \delta_{3j} z_t) b] = - \frac{\partial}{\partial \xi_j} \left( \frac{\tau_{ib}}{J} \frac{\partial \xi_j}{\partial x_i} \right), \quad \text{and} \quad (4d)$$

$$\frac{\partial}{\partial \xi_i} \left[ \frac{1}{J} \frac{\partial \xi_i}{\partial x_j} \frac{\partial \xi_m}{\partial x_j} \frac{\partial p}{\partial \xi_m} \right] = \mathcal{R}. \quad (4e)$$

Equation (4a) is the mass conservation (continuity) equation, (4b) is the geometric conservation law (GCL) governing the motion of the grid ([Thomas and Lombard 1979](#)), (4c) is the momentum transport equation, (4d) is the transport equation for a conserved scalar, and (4e) is the pressure Poisson equation. The right-hand sides of (4c) and (4d) are physical processes in the wave boundary layer, namely, pressure gradients and divergence of subgrid-scale fluxes.

The time dependence of the grid modifies the LES equations: the Jacobian appears inside the time tendency of each transport equation, and the total vertical flux of a variable  $\psi$  depends on the difference between the contravariant flux velocity and the grid speed  $(W - z_t)\psi$ . Examination of (4) shows that if the velocity and scalar fields are set to constant values then the left-hand sides of (4c) and (4d) reduce to (4b). Hence, the numerical method needs to satisfy the reduced form of the GCL discretely in order to prevent artificial sources and sinks from developing in the computational domain.

In our LES, the sidewall  $(x, y)$  boundary conditions are periodic, and the upper boundary condition is free slip with  $w = 0$ . The upper boundary  $\zeta = H$  is a level surface with  $\zeta_x = 0$ . The boundary conditions on the scalar are  $b \equiv b_s = 1$  at  $\zeta = 0$  and  $\partial b/\partial \zeta = 0$  at  $\zeta = H$ , and the initial scalar concentration profile is simply a constant  $b(x, y, z) = 0.8$ . The surface boundary condition for scalar concentration is idealized and neglects spray generation and streamwise modulation by waves as reported by [Peirson et al. \(2014\)](#). As is common practice with geophysical flows, at the lower boundary we impose rough wall boundary conditions based on a drag rule where the surface transfer coefficients are determined from Monin–Obukhov (MO) similarity functions ([Moeng 1984](#)). In the

present application, the MO rules are applied point by point at the lower boundary as described by Sullivan et al. (2014a) and Mironov and Sullivan (2016). The use of local surface exchange coefficients is an approximation but is supported by the analysis of Wyngaard et al. (1998).

We utilize well-established algorithms to integrate the LES equations (4). The equations are advanced in time using an explicit fractional step method that enforces incompressibility at every stage of the third-order Runge–Kutta (RK3) scheme. Dynamic time stepping with a fixed Courant–Friedrichs–Lewy (CFL) is used, and the spatial discretization is second-order finite difference in the vertical direction and pseudospectral in horizontal planes. Further algorithmic details are given by Moeng (1984), Sullivan et al. (1994, 1996), McWilliams et al. (1999), Sullivan and Patton (2011), Moeng and Sullivan (2015), and the references cited therein.

### c. Ensemble average model

The LES equations [(4)] are cast in strong conservation form. This form readily shows global conservation and thus can be used to develop a single column (or ensemble) model describing the balance of momentum and scalar fluxes in a wavy boundary layer. Spatial averaging of (4c) for streamwise momentum and (4d) for scalar concentration along wave-following surfaces (i.e., averaging along a surface of constant  $\zeta$ ), invoking horizontal periodicity, assuming a constant large-scale pressure gradient, and making use of metric identities leads to the ensemble average equations

$$\frac{\partial}{\partial t} \left\langle \frac{u}{J} \right\rangle = -\frac{\partial \mathcal{P}}{\partial x} - \frac{\partial}{\partial \zeta} \left\langle \frac{p}{J} \frac{\partial \zeta}{\partial x} + u(W - z_t) + \frac{\tau_{1k}}{J} \frac{\partial \zeta}{\partial x_k} \right\rangle, \quad \text{and} \quad (5a)$$

$$\frac{\partial}{\partial t} \left\langle \frac{b}{J} \right\rangle = -\frac{\partial}{\partial \zeta} \left\langle b(W - z_t) + \frac{\tau_{kb}}{J} \frac{\partial \zeta}{\partial x_k} \right\rangle. \quad (5b)$$

In the above,  $\langle \cdot \rangle$  denotes the horizontal spatial averaging operator, (5a) uses the identity  $\langle J \rangle = 1$  for our coordinate transformation, and the wave slope  $z_\xi = -\zeta_x/J$ . Under statistically stationary conditions, a vertical integral of (5a) from the water surface  $\zeta = 0$  to the top of the computational domain  $\zeta = H$ , a level surface with  $\partial \zeta / \partial x = 0$ , followed by application of the lower and upper boundary conditions on the contravariant flux velocity  $W = z_t$  (no flow through the boundary) leads to

$$-\frac{\partial \mathcal{P}}{\partial x} H \equiv u_*^2 = -\left\langle \frac{p}{J} \frac{\partial \zeta}{\partial x} + \frac{\tau_{1k}}{J} \frac{\partial \zeta}{\partial x_k} \right\rangle \Big|_{\zeta=0}. \quad (6)$$

As anticipated, (6) shows the bulk large-scale pressure gradient is balanced by a total surface drag  $u_*^2$ , which is a combination of form (or pressure) drag and SGS

stresses; (6) then defines the surface friction velocity  $u_*$ . In the LES implementation, the large-scale pressure gradient is conveniently written as  $-\partial \mathcal{P} / \partial x = u_*^2 / H$ . We use the ensemble average equations (5) and (6) to help guide the interpretation of the results in section 4.

## 3. Simulations

### a. Steady wave cases

The research target focuses on simulating turbulent airflow over steep waves featuring flow separation and wave breaking as observed in wind-wave flumes, for example, Banner (1990), Veron et al. (2007), Reul et al. (2008), and Buckley and Veron (2016). With this goal in mind, we impose synthesized wave shapes observed in a wind-wave tank by Banner (1990) as lower boundary conditions in the LES; see photographs in Fig. 1. In these experiments the wave fields are generated by an oscillating mechanical paddle in combination with the action of the wind. Two classes of steep waves are shown in the images of Fig. 1, namely, waves near the onset of breaking and waves with spilling flow down the forward face of the wave. We refer to these classes of steep waves as “incipient” and “active” breaking, respectively, in the following discussion. A brief summary of the observed wind and wave properties including the root-mean-square (rms) wave slope  $ak$  is given in Table 1; a detailed description of the experimental setup is provided by Banner (1990).

The available observations did not sample the complex multiscale instantaneous wave height  $h(x, y, t)$  observed in Fig. 1. For our LES modeling we simply adopt a spanwise (or  $y$ ) average view of the wave height  $h_s(x)$  that neglects the spanwise modulations in Fig. 1; that is, the wave height is assumed to be 2D. The wave inputs to the LES are prepared as follows: First, the wave shapes in Fig. 1 are projected onto an  $x$ – $z$  plane, digitized, and fit with a cubic spline. The beginning and ending points are lightly smoothed to create streamwise periodic functions  $h_s(x)$ . The resulting wave heights  $h_s(x)$  and wave slopes  $\partial h_s(x) / \partial x$  for the incipient and active breakers are shown in Fig. 2. The smoothed wave shapes in Fig. 2 retain the essential details of real waves; the waves are not monochromatic, featuring steeper peaks and shallower troughs as expected for wind waves. For the incipient breaker the local wave slope  $\partial h_s / \partial x \sim -0.25$  on the downwind face of the wave, while for the active breaker the wave slope is locally very steep  $\partial h_s / \partial x \sim -0.4$ , extending over a small area just forward of the wave crest. For later comparison we also compute turbulent flow over a monochromatic wave train with the same simulation design as the incipient case (described below) but with much lower rms wave slope  $ak = 0.071$ .



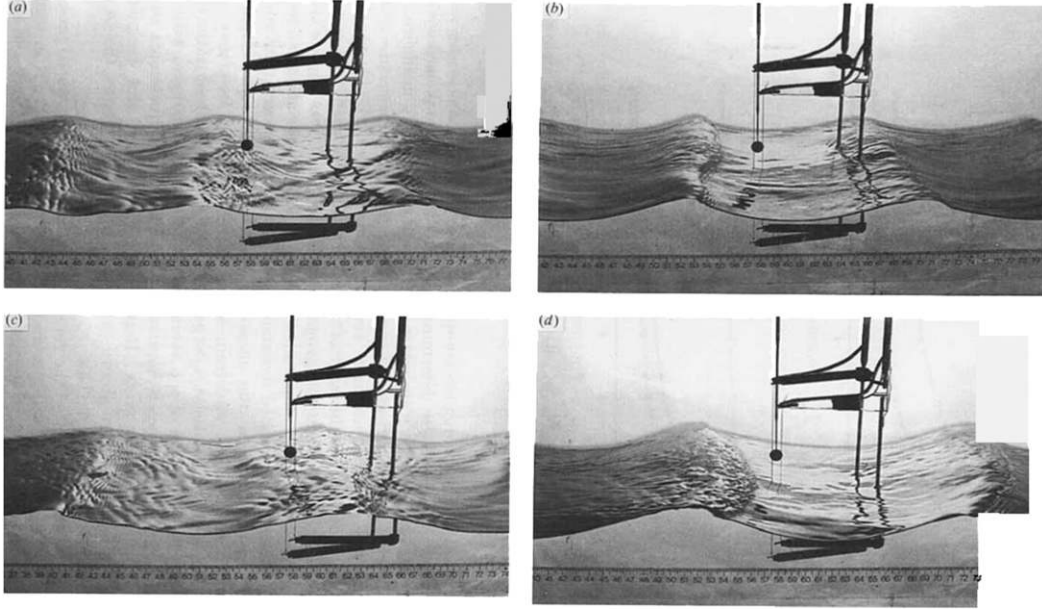


FIG. 1. Photographs showing steep waves observed in a wind-wave tank reported by [Banner \(1990, see his Fig. 8\)](#). (a),(c) The waves are near the onset of breaking (referred to as incipient). (b),(d) The waves are breaking (or spilling) down the wave front (referred to as active). Our simulations focus on the waves shown in (a) and (b).

The streamwise length of the LES computational domain needs to be periodic in terms of the wavelength  $\lambda$  of the imposed surface waves and at the same time sufficiently large to resolve low-wavenumber (large scale) turbulent motions. To satisfy both constraints the smoothed periodic wave shapes in [Fig. 2](#) are next replicated  $M$  times and stitched together in the  $x$  direction to form a long continuous periodic train of waves. The streamwise extent of the LES computational domain is then given by  $L_x = M\lambda$ , typically with  $M = 5$ . Cubic splines are used to interpolate the wave heights to the LES grid resolution.

The LES uses trigonometric basis functions and thus a complete wave train is represented by the discrete Fourier transform

$$\hat{h}_s(k_m) = \frac{1}{N_x} \sum_{i=1}^{N_x} h_s(x_i) \exp(-jk_m x_i), \quad (7)$$

where  $N_x$  is the number of grid points,  $k_m$  is the wave-number,  $x_i = (i - 1)/L_x/N_x$  are gridpoint locations, and  $j = \sqrt{-1}$ . To introduce time variations, the wave train is assumed to be quasi steady and propagate at a constant fixed phase speed  $c$  in the  $x$  direction. For the simulations, phase speed  $c$  and wavelength  $\lambda$  are assumed to obey the linear dispersion, and  $c^2 = g\lambda/2\pi$  with  $g$  equal to gravity, with values based on the peak measured wave as reported in [Table 1](#). At any future time  $\delta t = t - t_0 > 0$ ,

where  $t_0$  is the initial time when the waves are introduced, the wave height  $h(x, t)$  and wave slope  $\partial h/\partial x$  in the LES are given by

$$h(x_i, t) = \sum_{m=1}^{N_x} \hat{h}_s(k_m) \exp[jk_m(x_i - c\delta t)], \quad \text{and} \quad (8a)$$

$$\frac{\partial h(x_i, t)}{\partial x} = \sum_{m=1}^{N_x} \hat{h}_s(k_m) j k_m \exp[jk_m(x_i - c\delta t)]. \quad (8b)$$

The Fourier coefficients  $\hat{h}_s$  in (7) are evaluated once, stored, and reused in (8) as the simulations are advanced in time. Thus, the imposed waves propagate in time but with fixed shape.

The impact of surface drift velocity  $\mathbf{u}_d$  is also examined in the simulations because of its presumed link between breaking and airflow separation ([Banner and Melville 1976](#)). The total surface drift velocity  $\mathbf{u}_s$  was not measured in the experiments. We investigate the impact of  $\mathbf{u}_d$  according to the empirically based formula

$$\mathbf{u}_s(x) = \mathbf{u}_o(x) + \mathbf{u}_d(x), \quad (9)$$

TABLE 1. Measured wave properties.

Breaking wave state	$ak$ rms wave slope	$\lambda$ (m)	$c$ (m s <sup>-1</sup> )	$u_*/U_\infty$	$c/u_*$
Incipient	0.25	0.233	0.603	0.0693	1.58
Active	0.28	0.235	0.606	0.0896	1.23

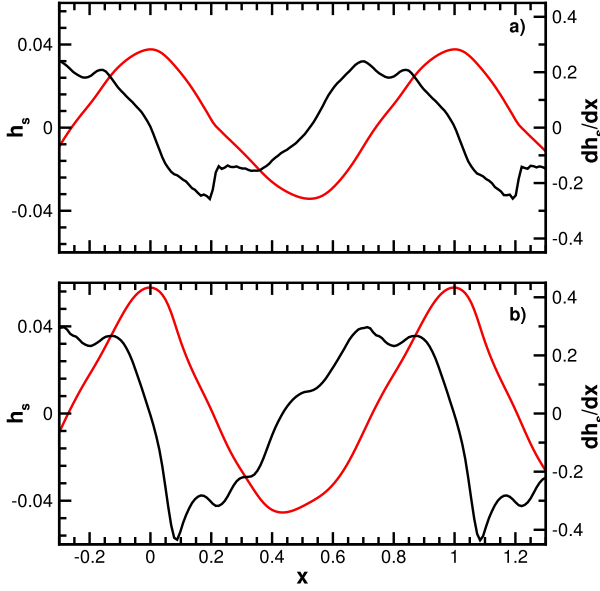


FIG. 2. Wave height  $h_s$  and wave slope  $dh_s/dx$  of the (a) incipient and (b) active breakers. In each panel, the wave height and wave slope are indicated by red and black lines with their vertical  $y$  axis indicated on the left and right sides of the figure, respectively. The wave height and alongwind distance  $x$  are made dimensionless by the wavelength given in Table 1.

where the wave orbital velocities ( $u_o, w_o$ ) are

$$\mathbf{u}_o(x) = \frac{h_p \pi c}{\lambda} [\cos(2\pi x/\lambda), \sin(2\pi x/\lambda)], \quad (10)$$

and

$$\mathbf{u}_d(x) = \gamma[1 + \cos(2\pi x/\lambda)][1, 0]. \quad (11)$$

The magnitude of the wave orbital velocities is estimated based on the measured wavelength  $\lambda$ , the computed phase speed  $c$ , and the maximum wave amplitude; that is,  $h_p$  is the distance between the wave crests and wave troughs in Fig. 2.

The empirical constant  $\gamma$  in (11) controls the magnitude and modulation of the surface drift  $\mathbf{u}_d$ . Based on wind drift levels reported in the literature (e.g., Wu 1975), the mean wind drift is approximately  $0.55u_*$ ; refined estimates are given by Peirson et al. (2014). Corresponding to the data in Banner (1990, his Table 2),  $u_* \sim 0.42 \text{ m s}^{-1}$ , which results in a mean wind drift of  $0.23 \text{ m s}^{-1}$ . To assess the likely sensitivity to the surface wind drift  $\mathbf{u}_d$ , we initially assume the simple cosine distribution in (11) using  $\gamma = 0.23 \text{ m s}^{-1}$ . This captures the mean wind drift and emulates its known amplification at wave crests (Phillips 1977, his section 3.9). The drift  $\mathbf{u}_d$  can be a substantial increment to the orbital velocities, for example, at the wave crest ( $u_o, u_d$ )/ $u_* \sim (0.44, 0.93)$

for the active breaker. As discussed below, the insensitivity of the results to  $\mathbf{u}_d$  precluded the need for a more detailed form of the drift distribution. In the LES, the drift velocity appears in the wavy surface boundary condition, specifically in the relative wind vector  $\delta \mathbf{u}$  used in the computation of the surface stress;  $\delta \mathbf{u}$  is the difference between the winds at the first model level above the water surface and the surface fluid velocity  $\mathbf{u}_s$ . These formulas relating surface stress to the winds at the first model level and the underlying currents are found in the appendix of Sullivan et al. (2014a). Simulations are performed with and without surface wind drift  $\mathbf{u}_d$  but always included the wave orbital velocities  $\mathbf{u}_o(x)$  in the surface velocity  $\mathbf{u}_s(x)$ .

The LES is formulated as a high-Reynolds number model of turbulent flow above a rough boundary and thus requires a surface roughness  $z_{o,s}$  as part of its wall modeling. In the LES,  $z_{o,s}$  is interpreted as the subgrid-scale unresolved surface roughness riding on top of the resolved waves. Based on the measured wind profiles above wind ripples, no paddle waves, Banner (1990, see his Table 2) estimates the surface roughness solely caused by the wind ripples as  $z_{o,s} \sim 0.078 \text{ mm}$ . For our computations we use a constant value  $z_{o,s} = 0.1 \text{ mm}$ . Thus, the nondimensional roughness  $z_{o,s}/\lambda \sim 4.3 \times 10^{-4}$  in all simulations. Using a standard value of air viscosity  $\nu_a$  and the measured values of  $u_*$ , this value of  $z_{o,s}$  is consistent with the assumption of a fully rough surface  $u_* z_{o,s}/\nu_a > 2.3$  suggested by Donelan (1998).

The LES design is picked to model turbulent airflow in the wind-wave tank setup shown in Fig. 1. For our steady wave experiments, a computational domain  $(L_x, L_y, H) = (5, 5, 1)\lambda$  is chosen based on sensitivity tests using different size domains, our past experience with direct numerical simulations of turbulent flow over waves in a Couette configuration (Sullivan et al. 2000; Sullivan and McWilliams 2002), and a related LES modeling study of airflow over monochromatic waves of steepness  $ak = 0.226$  (Hara and Sullivan 2015). Two different grid meshes are considered: a coarse grid with  $(N_x, N_y, N_z) = (256, 256, 128)$  grid points with horizontal spacing  $\Delta x = \Delta y = 0.0195\lambda$  and a 4 times finer horizontal grid of  $(512, 512, 128)$  grid points with spacing  $\Delta x = \Delta y = 0.0097\lambda$ . A smoothly stretched vertical grid with constant spacing between two neighboring grid cells is used in computational space. In terms of the computational vertical coordinate  $\zeta$ , the stretching factor  $K = \Delta \zeta_k / \Delta \zeta_{k-1} = 1.00282$  with the first grid cell positioned at  $\Delta \zeta_1 = 0.0065\lambda$ . As shown later in section 4, the differences between the coarse and fine mesh results are small with the fine grid results closely matching the observed wind profiles.

For generality, the simulations are performed in nondimensional units where all length and velocity

scales are made dimensionless by the wavelength  $\lambda$  and friction velocity  $u_*$ , respectively;  $u_*$  is defined in (6). Thus, in the simulations the nondimensional time unit  $t = Tu_*/\lambda$ , and the dimensionless large-scale pressure gradient  $-\partial\mathcal{P}/\partial x = 1$ . The passive scalar is dimensionless by design.

All simulations are initiated with turbulent flow fields archived from an LES above a slightly heated flat surface. The surface waves are gradually introduced over a short time period  $t \sim 0.25$  (about 1200 time steps), and the calculations are then continued for a time period  $t \sim 50$  (nearly 200 000 time steps). We emphasize that the calculations are done in a fixed horizontal frame of reference, that is, the computational grid is not translating horizontally with the phase speed of the waves. The waves continually propagate through the computational domain in the streamwise direction according to the prescription (8a). Statistics are continually monitored during the simulation. Based on the time series of the total surface drag, the flow is judged to reach a quasi-stationary state near  $t \sim 25$ ; see later discussion in section 4. Statistics are collected by time averaging over the last 25 time units of the simulation (about 100 000 time steps). At any particular time step, spatial averages are also formed by averaging along horizontal surfaces at constant  $\zeta$ , that is, along wave-following coordinate lines. A combined space–time average is indicated by  $\langle \cdot \rangle$ ; a turbulent fluctuation is denoted by  $(\cdot)'$ . Then any variable  $f$  is decomposed as  $f = \langle f \rangle + f'$ .

### b. Unsteady wave cases

We extend our LES study over steady, steep uniform wave trains to conditions more representative of natural waves, which typically occur as unsteady evolving wave groups (Longuet-Higgins 1984). This allows us to diagnose the potential significance of unsteadiness in the wave group structure on the overlying turbulent wind fields and most importantly on the surface pressure distribution and form drag. For our study, we adopt an unsteady space–time-evolving 2D chirped wave packet generated by the fully nonlinear wave tank code WSIM described by Grilli et al. (2001) and Banner et al. (2014). Details of the packet generation using WSIM are provided in the appendix. The chosen wave packet contains nine carrier waves in the space–time evolving group. The mean carrier wave steepness is intermediate, but its local maximum steepness becomes high during the evolution but always remains below the breaking onset. A robust reference packet wave speed  $c$  is deduced from the temporal and spatial spectrum of the packet elevation at a set of different streamwise locations. The resulting mean spectral peak frequency or peak wavenumber are used in the linear dispersion

relation for gravity water waves to provide further estimates of the corresponding spectral peak wave speed  $c$ . We also compute  $c$  as the direct ratio of mean peak frequency over mean peak wavenumber. All the various measures of  $c$  agree within a few percent. The space–time structure of the packet for wave age  $c/u_* = 1$  at selected LES time stamps during its evolution is shown below in Fig. 14. The maximum (most negative) wave slope of the packet varies from  $-\partial h/\partial x = [0.1, 0.35]$ , which spans the wave slope range covered by the steady incipient and active breakers.

In the LES experiments, we impose a single unsteady wave packet at the lower boundary and investigate very strong wind forcing with  $c/u_* = 1$ . The recipe for ingesting a wave packet in the LES is as follows: First, WSIM is run as an offline calculation for a complete life cycle of the 2D chirp packet with the calculations performed in nondimensional units: the packet's characteristic velocity and length scales ( $c, \lambda$ ) are used for nondimensionalization. Therefore, wave age is the conversion factor connecting the nondimensional chirp time  $\tilde{t} = Tc/\lambda$  and the LES time  $t = \tilde{t}u_*/c$ . The space–time volume of wave heights  $h(\tilde{x}, \tilde{t})$  from WSIM are archived at 2048 time stamps over a total time period  $\tilde{t} \sim 15$  discretized at 512 equally spaced grid locations with spacing  $\Delta\tilde{x} = 0.0237$ . The streamwise extent of the LES domain is chosen to capture the packet evolution. The complete LES computational domain  $(L_x, L_y, H) = (9.40, 4.695, 1)$  is discretized on a grid with  $(N_x, N_y, N_z) = (1024, 512, 128)$  grid points. In terms of the characteristic packet wavelength, the horizontal resolution in the LES is  $\Delta x = \Delta y = 0.00916\lambda$ . This is slightly finer mesh spacing compared to the resolution used in the steady simulations. In terms of the  $\zeta$  coordinate, the vertical distribution of grid points is identical between steady and unsteady cases.

To use the WSIM results in LES, we need to employ space–time interpolation (e.g., Sullivan et al. 2014b) and account for the difference in time normalization caused by wave age. First, at all available WSIM time stamps the wave heights are interpolated to the LES grid locations using standard cubic splines, which are subsequently lightly tapered at the start and end to ensure a spatially periodic wave form over the streamwise length  $L_x$ . These results are stored in a separate data volume that is input externally to the LES code. The LES time stepping is adaptive, and hence the LES time stamps are unknown a priori and of course do not match the WSIM time locations. To determine wave heights at the LES time stamps we employ temporal interpolation using a local in time Catmull–Rom spline (Catmull and Rom 1974). This spline is efficiently implemented on the fly and exactly matches the wave height and wave slope

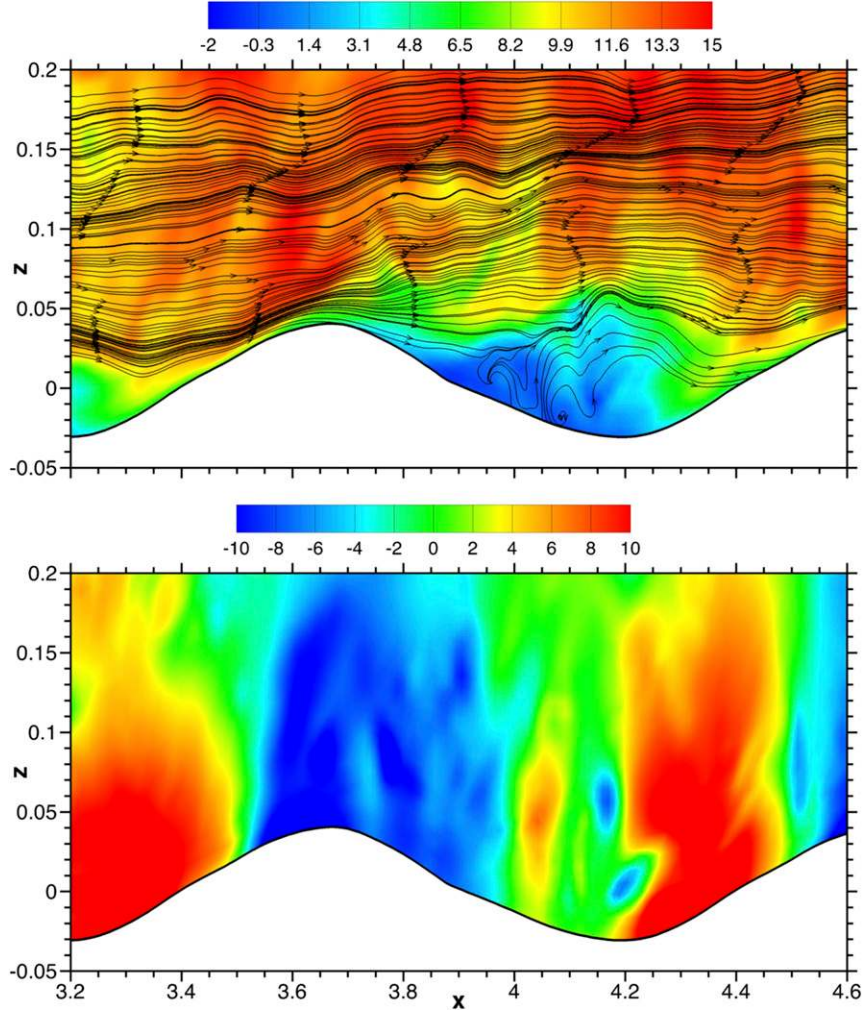


FIG. 3. A snapshot of instantaneous fields in an  $x$ - $z$  plane for flow over an incipient breaker. In the upper panel, streamlines, generated from the instantaneous vector field  $[u(x, z), w(x, z)]$ , overlay color contours of streamwise velocity  $u$ . The lower panel shows contours of pressure fluctuations  $p$ . Only a fraction of the horizontal and vertical domains is displayed and the aspect ratio of the plots is not unity. The wind and wave propagation directions are from left to right.

from WSIM using only four local control points. The spline fits to the wave height are used to compute the space and time derivatives ( $\partial h/\partial x$ ,  $\partial h/\partial t$ ), which are required in the LES. These derivatives are used to determine the grid speed  $z_t$  and also appear in the computation of the surface orbital velocities ( $u_o$ ,  $w_o$ ):

$$\frac{\partial h}{\partial t} = w_o - u_o \frac{\partial h}{\partial x}. \quad (12)$$

We estimate  $u_o$  based on the semilinear approximation for nonlinear waves described and evaluated by Grue et al. (2008).

Inspection of the WSIM output shows that the packet focusing, and hence rapid growth, only begins late in its life cycle. Since we are primarily interested in the turbulent

winds under packet focusing, we initiate the LES calculations at the WSIM time stamp  $\tilde{t}_o = 11.69$ , with the LES computations spanning the interval  $t = [0, 3.27]$ , that is,  $t = \tilde{t} - \tilde{t}_o$ . For  $c/u_* = 1$ , approximately 17 000 LES time steps are needed to cover this time interval. Similar to the simulations over steady waves, the LES over the unsteady chirp packet is initiated with mean winds and fully developed turbulence archived from a separate simulation above a flat surface.

## 4. Results for steep steady waves

### a. Instantaneous fields

Extensive visualization of the 3D instantaneous velocity, pressure, and vorticity fields is employed to detect



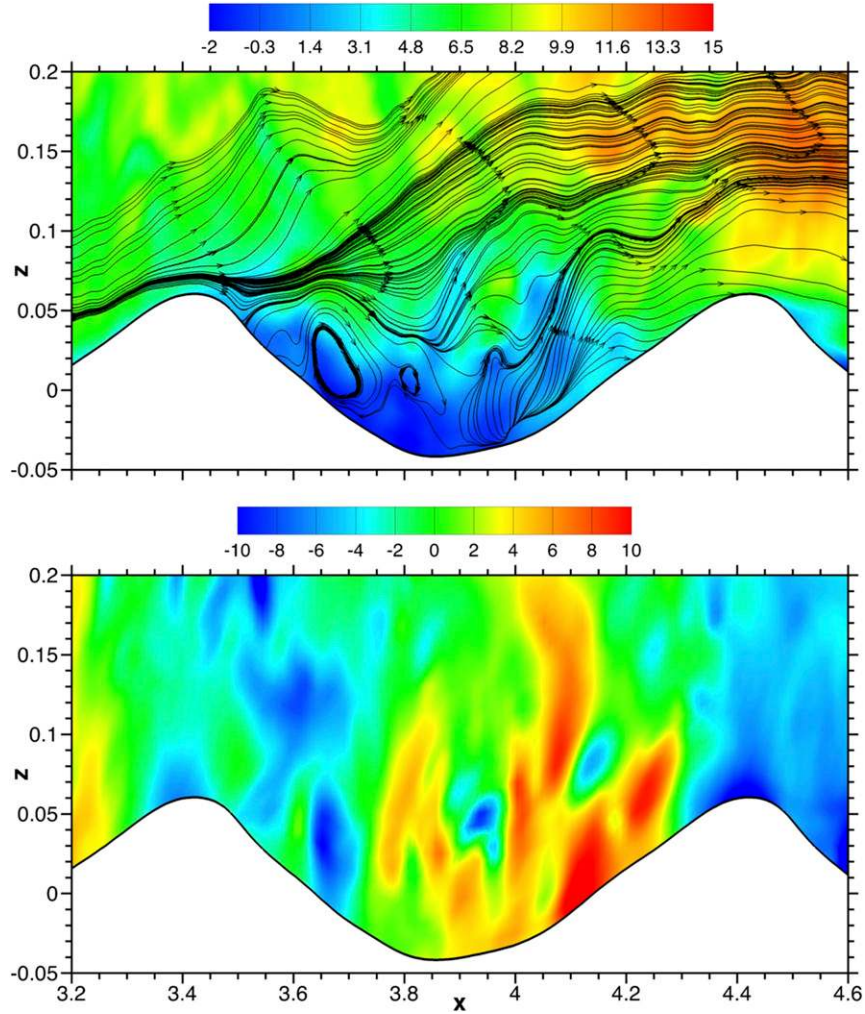


FIG. 4. As in Fig. 3, but for flow over an active breaker.

airflow separation in the simulations. Typical images highlighting the spatial distribution of the near-surface velocity and pressure fields for the incipient and active breaker simulations are displayed in Figs. 3 and 4, respectively. Companion images of the vorticity fields, described later, are shown in Figs. 9 and 10. We emphasize that all the visualizations are presented in a fixed frame of reference, similar to experimental results (e.g., Veron et al. 2007), with winds and waves propagating left to right. And we are fully aware that caution is needed in interpreting the patterns of streamwise velocity since the winds and the underlying waves are both propagating in the  $x$  direction.

All images illustrate signatures of airflow separation and its consequences for the pressure field over these strongly forced moving waves. Notice the instantaneous streamlines, formed from the vector field  $[u(x, z), w(x, z)]$ , detach (lift off) near a wave crest and evolve

into elevated shear layers in the outer flow. Second, the streamwise  $u$  contours are negative in the wave trough, further indicative of recirculating backflow. In the active breaker simulation, the nearly closed contours of the streamlines in the wave trough result from complex vortical motions (also see Fig. 10 below). Our instantaneous velocity streamlines with airflow separation are in agreement with those described by Veron et al. (2007) and Reul et al. (2008), observed over steep waves.

Although the flow patterns in Figs. 3 and 4 are similar they differ in the details of the airflow separation, which impacts the surface drag (see section 4b). In the less steep incipient case, the separating flow often leaves a wave crest, skips over the wave trough, and reattaches on the upwind face of the downstream wave, nearly decoupling the trough flow from the outer flow; the stagnating flow on the downstream wave generates high positive fluctuating pressure, as shown in Fig. 3.

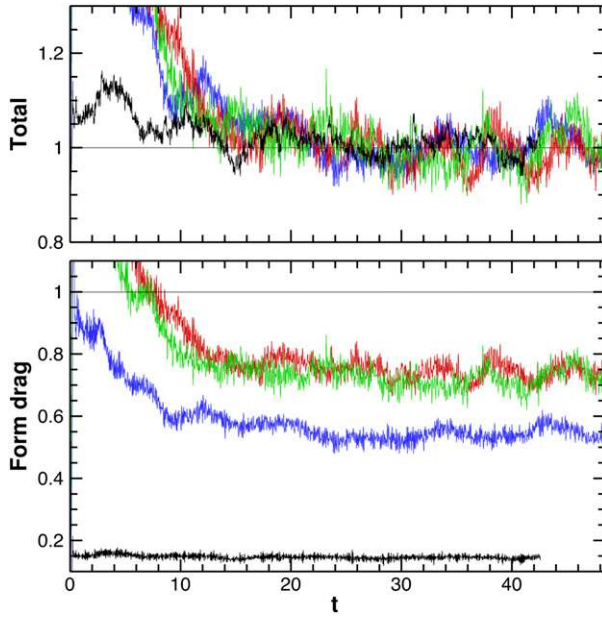


FIG. 5. (top) Temporal variation of the computed total surface stress and (bottom) the contribution from the form stress (or pressure drag). In each figure stresses are normalized by the friction velocity  $u_*^2$ . Cases are active (red), incipient (blue), monochromatic low wave slope (black), and an incipient case with rms wave slope matching the active case (green).

Meanwhile in the active case, the flow separation generates a much broader downstream wake. In the example of Fig. 4, the extensive slow-moving fluid and fluid ejections from the wave trough deflect the separating streamlines far from the wave boundary. Also, the surface pressure field is less spatially coherent across the wave surface. Broadly, the airflow separation over these steep waves is qualitatively similar to separating turbulent flow over a backward-facing step, a rectangular cavity, or the thin shear layers that develop over streamlined bodies (e.g., Szubert et al. 2015). However, in the present flow the shear layers that separate from the wave surface, although initially thin, expand vertically and propagate into the outer flow with increasing downstream distance because of background turbulence.

#### b. Drag and pressure distributions

The bulk balance of momentum fluxes given by (6) is an informative diagnostic for judging the stationarity of the LES solutions and also demonstrates how the total stress is decomposed into form and SGS (or viscous) drag. Figure 5 displays the temporal variation of the computed total stress (top panel) and the fraction of the total stress that is supported by form stress  $\langle p\partial h/\partial x \rangle$  (bottom panel). Recall the simulations are performed in

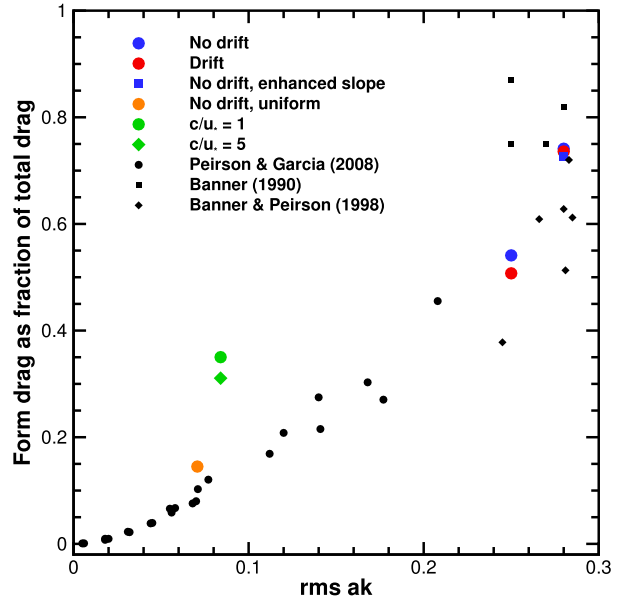


FIG. 6. Form (pressure) drag for LES cases with steady and unsteady waves. Results for the incipient and active breaking waves with varying surface drift are shown with red and blue dots. The incipient case with its wave slope enhanced to match the active case is shown by a blue square; its form drag is nearly identical to that obtained in the active breaker case. The form drag of a monochromatic uniform wave train with low rms wave slope  $ak = 0.071$ , and no surface drift is indicated by an orange dot. The form drag of an unsteady wave packet with rms wave slope  $= 0.084$  and  $c/u_* = (1, 5)$  (see section 5) are indicated by a green dot and diamond, respectively. The solid black symbols are measurements collected over the wave age range  $c/u_* < 5$ .

nondimensional units using velocity and length scales  $(u_*, \lambda)$ , and with this normalization the computed stresses are compared relative to unity. As might be expected the simulation of turbulent flow over a train of monochromatic waves of low wave slope and no flow separation reaches a stationary state sooner than the steep wave simulations; that is, the low wave slope simulation can be considered stationary starting at say  $t \sim 10$ . The flow over steep waves is judged to be quasi stationary at  $t > 20$  based on the nearly equal amplitude of the positive–negative oscillations of the total stress about unity. We find these oscillations are induced by intermittent flow separation and reattachment (see section 4a). The sharp change in total stress between  $0 < t < 20$  in flow over steep waves is a transient caused by the initial turbulence being in disequilibrium with the surface wave field. Figure 5 (bottom panel) and Fig. 6 highlight the form stress changes with varying wave slope. Notice that with low wave slope  $ak = 0.1$ , and the form stress is approximately 12% to 15% of the total drag; this is in good agreement with previous DNS results for waves of similar wave age  $c/u_* \sim 1$

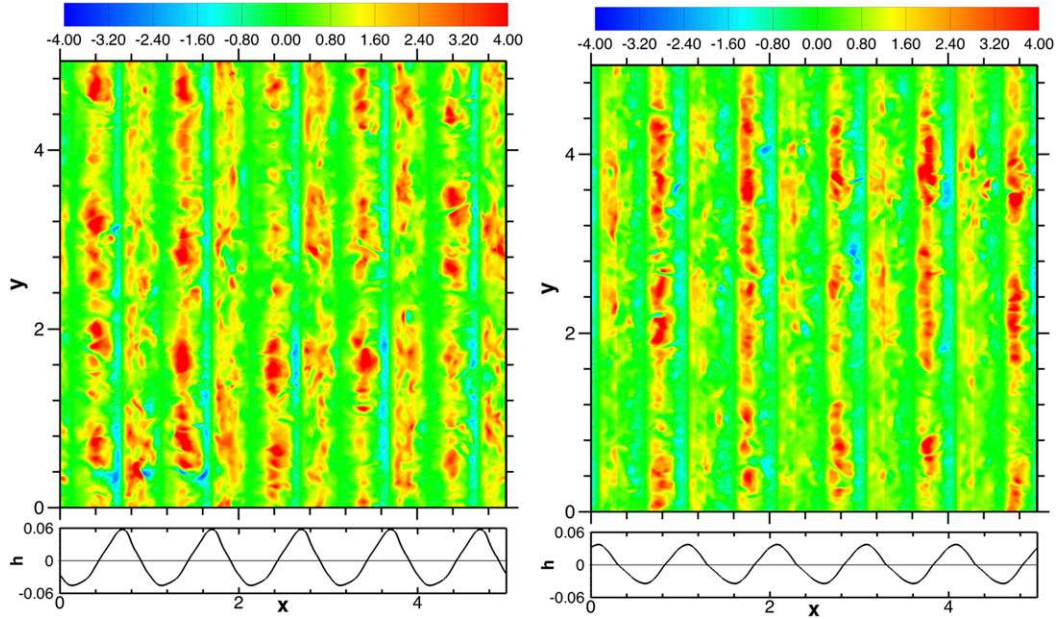


FIG. 7. Instantaneous contours of pressure-wave slope correlation  $\overline{p\partial h/\partial x}$  in an  $x$ - $y$  plane for (left) active and (right) incipient breaking. For reference, the two-dimensional wave height  $h(x, t)$  is shown in the bottom of each panel. The winds and waves both propagate from left to right. A large fraction of the total form drag occurs on the windward face of the waveform, that is, where positive pressure is well correlated with positive wave slope. The red contours are regions where the local pressure drag is more than 5 times the mean value.

(Sullivan et al. 2000) and from second-order closure models (Li et al. 2000). With increasing steepness the fraction of form stress grows appreciably with the fraction  $\sim(54\%, 74\%)$  of the total stress for incipient and active cases, respectively. In the wind-wave experiments, Banner (1990) reports that the total drag in dimensional units increases dramatically by a factor of 2 between the incipient and active breaker cases.

One of the key questions we wish to investigate is the role of wave steepness versus wave breaking in setting the level of form drag. In other words, is the enhanced form drag in Fig. 5 a consequence of flow separation or wave breaking? These effects are difficult to isolate in measurements as both processes appear and often concurrently, for example, Veron et al. (2007) and Reul et al. (2008). To explore these ideas we artificially increase the wave height of the incipient breaker by a factor  $\chi = 1.45$ , such that its overall rms steepness closely matches that of the active breaker. This is not a definitive test but serves to isolate wave steepness from wave breaking effects. Results are displayed in Figs. 5 and 6. Boosting the rms wave slope of the incipient breaker elevates the form stress contribution and generates temporal oscillations in the total drag that nearly match the active breaker simulation. The impact of the surface drift parameterization [(11)] on form drag is summarized in Fig. 6. In both the incipient and active

breaker simulations, including an enhanced surface drift has only a small impact on the form drag levels. These parameter variations suggest that the magnitude of the overall wave steepness is the critical wave property for inducing large form drag over steep steady waves. The LES estimates of form drag fraction for rms  $ak = (0.071, 0.25, 0.28)$ , shown in Fig. 6, agree well with the laboratory estimates of Banner (1990), Banner and Peirson (1998), and Peirson and Garcia (2008) for strongly forced waves.

The enhanced form drag over steep waves is ultimately buried in the pressure wave slope correlation. A typical horizontal spatial distribution of  $\overline{p\partial h/\partial x}(x, y)$  at late time for incipient and active breakers is shown in Fig. 7. First, even though the imposed surface field is 2D and propagates steadily, the pressure wave slope correlation is both spatially and temporally intermittent, owing to the fluctuations in the overlying turbulent air-flow. Notice that regions just forward of the wave crest are major contributors to the form drag. In this region negative fluctuating pressure is strongly correlated with negative wave slope and thus  $\overline{p\partial h/\partial x} > 0$ . However, also notice an even larger fraction of the drag is supported on the forward face of the downstream wave; in this region positive fluctuating pressure is well correlated with positive wave slope and thus again  $\overline{p\partial h/\partial x} > 0$ . Flow visualization of the velocity fields in  $x$ - $z$  planes (see

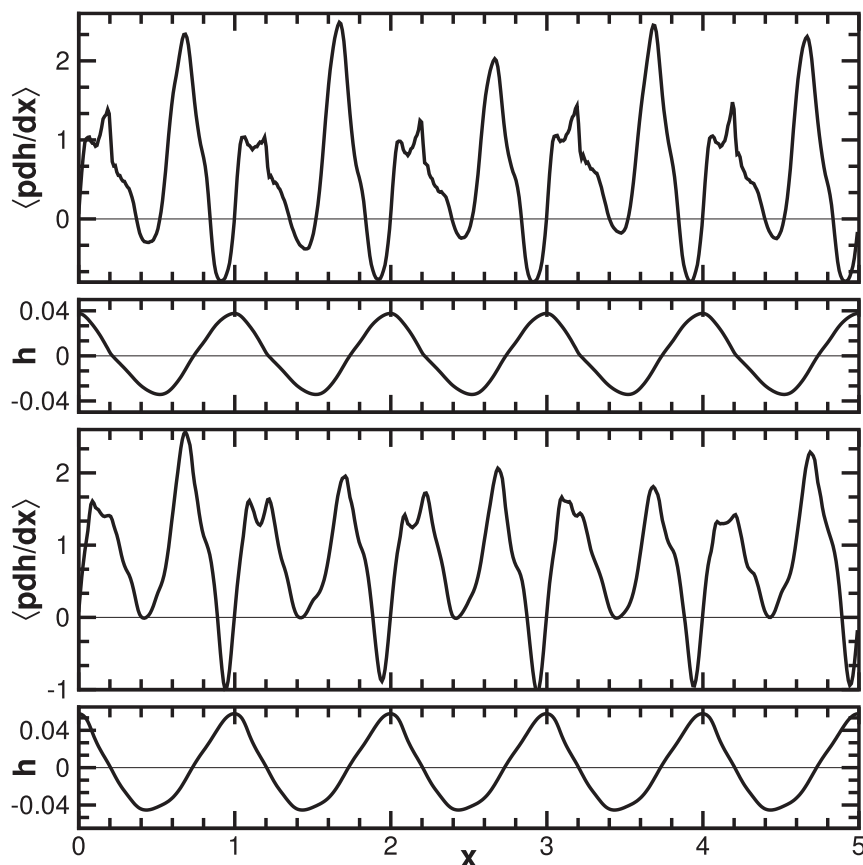


FIG. 8. Form drag at the wave surface obtained by  $y$  averaging the results in Fig. 7. Results for the incipient and active breaker fields and the corresponding wave height  $h(x, t)$  are shown in the upper two and lower two panels, respectively.

Figs. 3, 4) shows that the flow often separates intermittently near the wave crest, then skips over the wave trough, and subsequently reattaches on the forward face of the downstream wave; that is, intermittent reattachment of the separating flow creates a stagnation point (or a splat) on the face of the downstream wave, which is corroborated by the experimental results by Banner and Peirson (1998). Similar splats are also observed in flow over periodic steep stationary hills by Henn and Sykes (1999) and result in an enhancement of the local spanwise velocity  $v'$ . The other key factor to observe in Fig. 7 is the pressure-wave slope correlation is episodic with magnitudes nearly 5 times the average drag  $u_*^2$ . Large voids are, of course, observed in the wave trough and crest where  $\partial h / \partial x \rightarrow 0$ .

The spanwise (or  $y$ ) average of the pressure-wave slope correlation quantifies which part of the wave field supports form drag. Figure 8 shows that a large fraction of the form drag over steep waves is generated at the reattachment stagnation location. The peaks in  $\langle p \partial h / \partial x \rangle_y$  on the downstream wave face are nearly identical for

incipient and active breakers. The extra drag for active breakers comes from an enhancement slightly downwind of the wave crest. While the separation zone is frequently the focus of many studies, from a drag perspective the reattachment splat regions are clearly important.

To add confidence to the hypothesis that flow separation occurs over moving waves it is important to examine Galilean invariant flow fields (e.g., Veron et al. 2007; Reul et al. 2008). Figures 9 and 10 show typical instantaneous contours of spanwise vorticity  $\omega = \partial u / \partial z - \partial w / \partial x$ , computed in transformed coordinates, for the incipient and active breakers, respectively. We notice on the windward face of the waves the vorticity is positive signed and tightly compacted in a very thin near-surface layer, for example, just upwind of the wave crests near  $x \sim [1, 2]$  in the incipient case and  $x \sim [1.2, 4.2]$  in the active breaker case. Thus, the flow is attached to the wave surface in this region. Near or slightly forward of the wave crests, a sheet of concentrated vorticity lifts off (separates) from the water surface, generating an



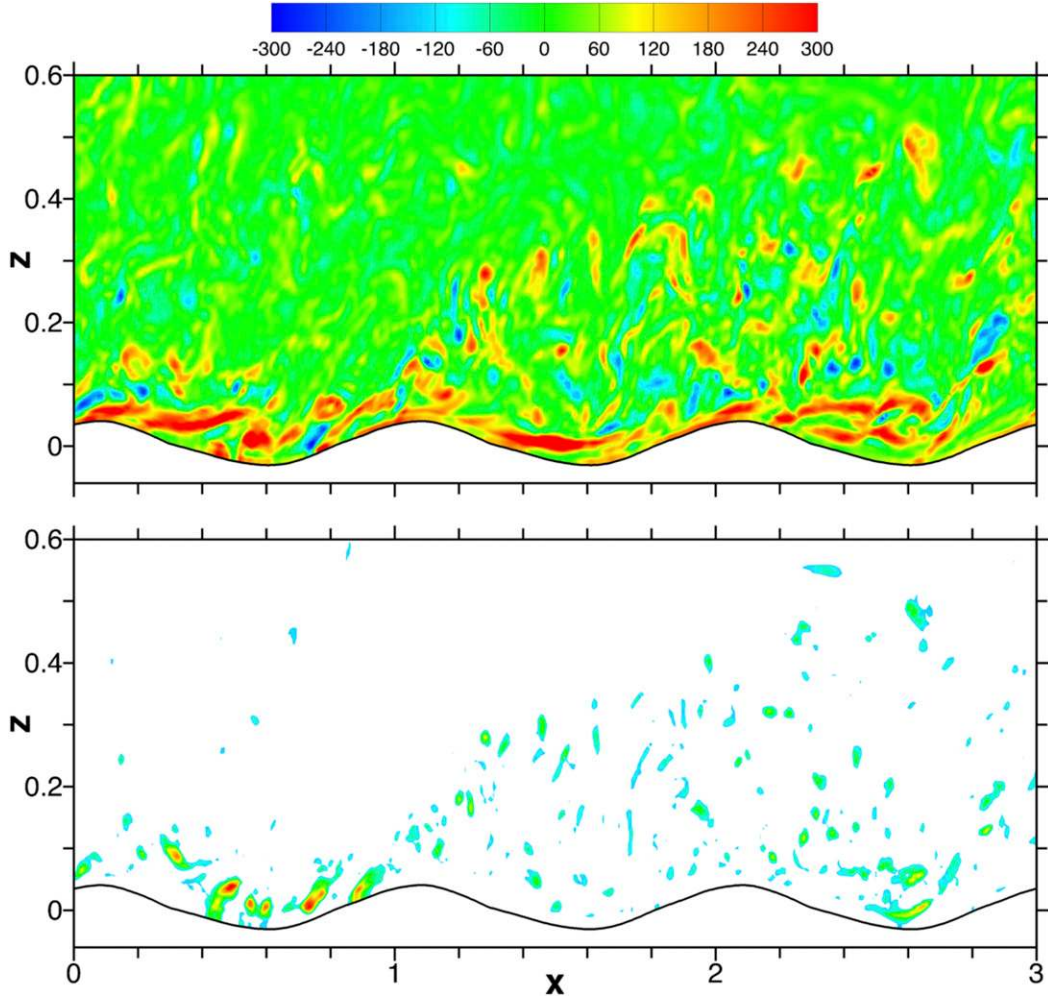


FIG. 9. (top) Snapshot of instantaneous spanwise vorticity  $\omega \hat{y}$  contours in an  $x$ - $z$  plane from LES over a train of incipient breakers. A vigorous (positive signed) vorticity layer is attached to the forward face of the waves, for example, near  $x \sim 0.9$ . This vorticity layer separates from the wavy surface forward of the wave crest propagating into the overlying turbulent flow. (bottom) The vorticity/shear layer contains strong vortices. The vortical cores are identified by the complex eigenvalues of the velocity gradient matrix  $\partial u_i / \partial x_j$ , that is, the so-called  $\lambda_{ci}$  method of Zhou et al. (1999). Colored swirl contours with values larger than 25% of the maximum swirl are shown; smaller swirl values simply appear white. The swirl contours are distorted by the  $x$  and  $z$  plotting scales. For clarity, only a fraction of the streamwise  $x$  domain is shown in the images.

energetic shear layer in the outer flow disconnected from the boundary. Downstream of the separation location, the separating vorticity/shear layer breaks up into zones of positive and negative signed spanwise vorticity that propagates upward into the turbulent wave boundary layer, for example, up to  $z \sim 0.6$ . In the active breaker simulation, vorticity/shear layers occur more often and can be spotted separating from the water surface just forward of nearly every wave crest. Then a vigorous vortical layer fills the vertical domain between the wave surface and  $z \leq 0.2$  spanning multiple crest–trough–crest regions. Qualitatively these images are remarkably similar to those obtained from

PIV measurements in wind-wave tanks by Veron et al. (2007) and Reul et al. (2008).

Next, we apply the so-called  $\lambda_{ci}$  vortex extraction technique (Zhou et al. 1999) to the near-surface flow fields in order to identify vortical structures in the separated vorticity/shear layers. The lower panels of Figs. 9 and 10 show contours of  $\lambda_{ci}$  or nondimensional flow “swirl.” The closed contours indicate the separating vorticity layers in the upper panels of Figs. 9 and 10 are indeed composed of numerous vortex cores with their axes aligned with the  $y$  direction. These results strongly suggest that airflow separation is a dominant mechanism in our simulations and occurs over both incipient and

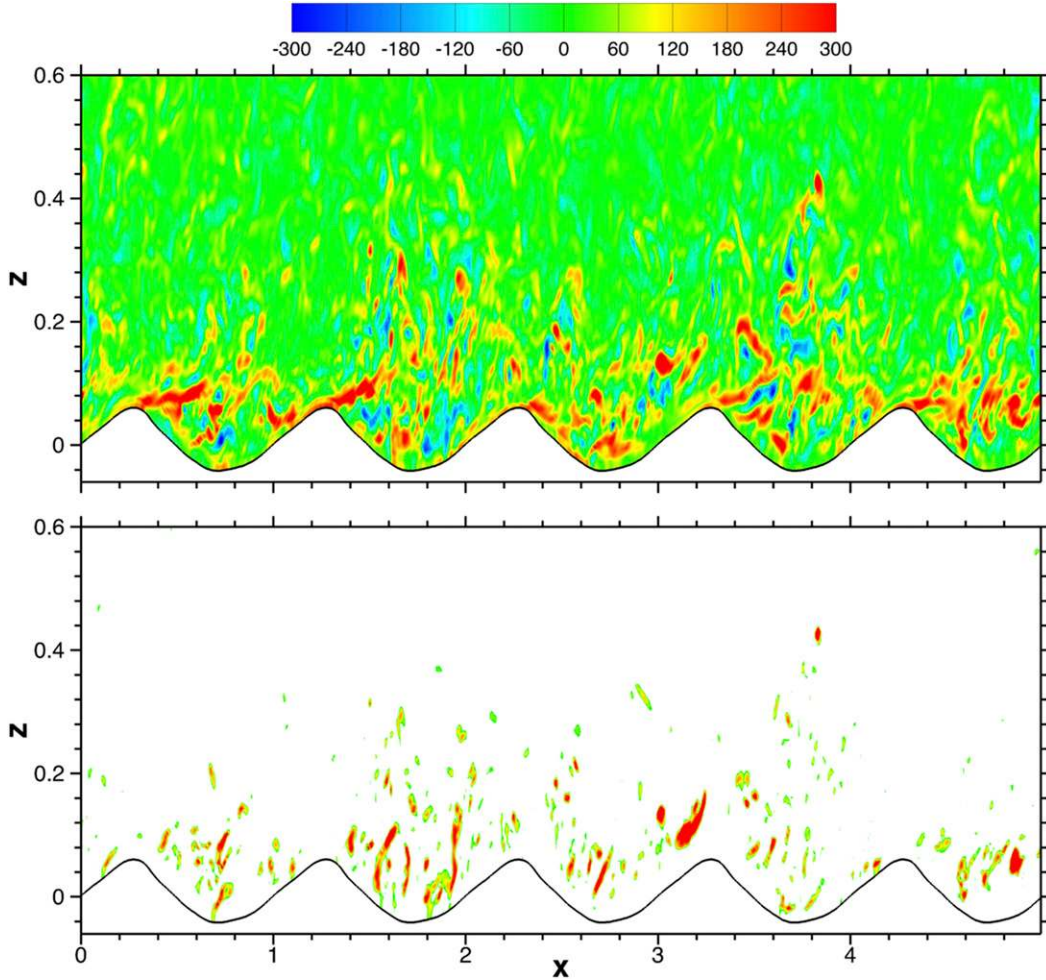


FIG. 10. (top) Snapshot of instantaneous spanwise vorticity  $\omega \hat{y}$  contours in an  $x$ - $z$  plane from LES over active breakers, for comparison with the incipient case see Fig. 9. (bottom) The vortical cores in the vorticity/shear layers separating from the wave crests using the same coloring scheme as in the lower panel of Fig. 9. In these images, contours are shown over the full extent of the streamwise computational domain  $L_x$ .

active breakers. Also, the results indicate airflow separation is temporally and spatially intermittent and likely occurs before the onset of breaking. Thus, the criterion for airflow separation over moving waves suggested by Banner and Melville (1976) and Gent and Taylor (1977), which is based on ensemble averages and does not account for turbulent fluctuations in the overlying airflow and boundary movement (Miron and Vétel 2015), is likely too strict; that is, their criterion guarantees separation but is not necessary.

Critical layer mechanics, that is, the flow dynamics at the vertical level where wind speed matches the phase speed of the underlying wave  $\langle u \rangle \sim c$ , is a key concept used to estimate wave growth for a spectrum of waves (e.g., Belcher and Hunt 1998; Hristov et al. 2003; Janssen 2008; Grare et al. 2013a). In our simulations, based on the logarithmic law for velocity

(Phillips 1977, p. 128), we estimate that the critical level is at most  $\zeta_c/\lambda \sim 8 \times 10^{-4}$  for wave age  $c/u_* = 1.58$  and wind ripple roughness  $z_{o,s}/\lambda \sim 4.3 \times 10^{-4}$ . Thus, in the simulations  $\zeta_c/\lambda$  is collapsed down to the water surface well below the first vertical grid level in the LES. For our strongly forced waves there is no signature of a critical layer very near the surface, and apparently the critical layer has a marginal influence on the pressure distribution and surface drag in the simulations.

### c. Velocity profiles and momentum budget

How well do statistics from the simulations match up with the available measurements of Banner (1990)? A comparison of the average boundary layer wind profiles  $\langle u \rangle/u_*$  as a function of distance above the waves in log-linear coordinates is shown in Fig. 11. It is important

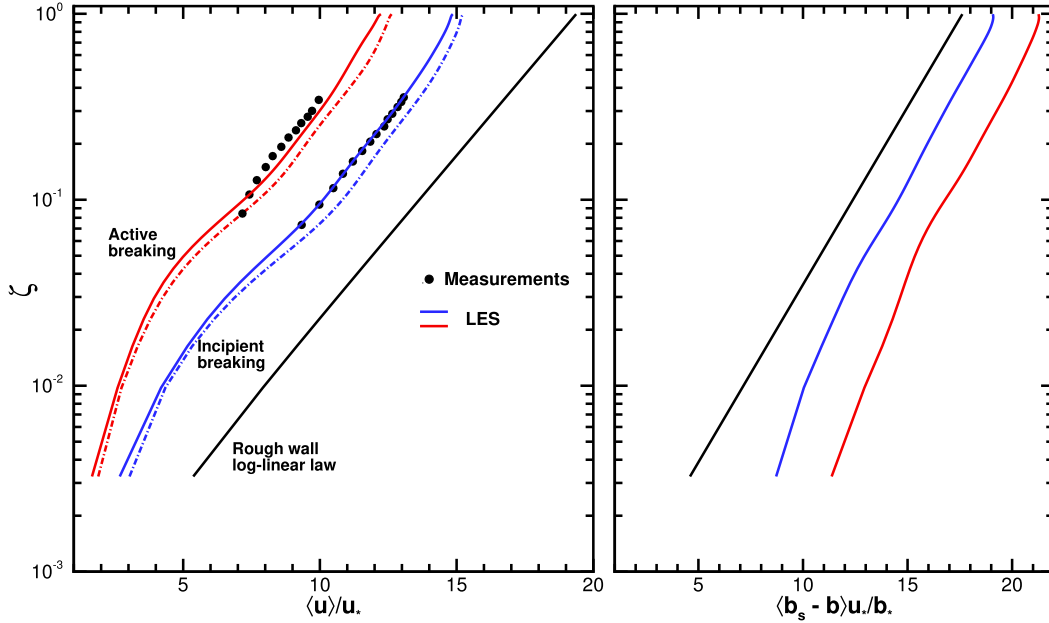


FIG. 11. Vertical profiles of (left) average streamwise wind and (right) scalar concentration difference for incipient (blue) and active breakers (red) from LES. In the left panel, the solid and dashed-dotted lines use grid meshes of  $(512^2 \times 128)$  and  $(256^2 \times 128)$  grid points, respectively. For reference, rough surface log-linear wind and scalar profiles for no resolved surface waves, wind ripples with  $z_o/\lambda = 10^{-4}$ , are also shown by a solid black line. At constant  $\zeta$ , the left shift of the wind profile  $\langle u \rangle / u_*$  reflects an increase in the bulk momentum roughness  $z_{o,m}$  induced by breaking waves. Solid bullets are measurements of mean wind speed from Banner (1990). The right shift of the scalar profile reflects a decrease in the bulk scalar roughness  $z_{o,b}$ .

to note the differences in data processing in this simulation–measurement comparison. First, the wind measurements are collected from probes located at fixed heights above the mean water surface (i.e., the probes are not wave following and hence there are no wind measurements below the wave crests). Meanwhile the wind profiles in the simulations are obtained by averaging in a wave-following frame of reference. These differences in frame of reference are minimized with increasing distance from the wave surface because the streamwise gridlines rapidly approach level surfaces with increasing  $\zeta$ , that is, as  $\zeta \rightarrow z$ . Second, the LES simulates flow in a periodic channel driven by a mean pressure gradient while the wind-wave tank setup produces a streamwise developing boundary layer flow (e.g., Gong et al. 1996, p. 24). Despite these inherent differences, we judge the wind profile comparison in the log-linear range as very good, especially for the fine mesh LES, which adds confidence to our interpretations of the LES flow fields. The LES wind profiles exhibit a slight sensitivity to the grid mesh. Apparently, a fine horizontal mesh with  $\Delta x \leq 0.01\lambda$  is required to resolve the separation and reattachment locations.

The underlying surface waves leave a significant imprint on the LES wind profiles. Broadly, the velocity profile over resolved steep waves consists of a roughness

sublayer (say  $\zeta < 0.05$ ) and a log-linear layer (say  $\zeta > 0.1$ ) patched together by an intermediate transition zone. Thus, at our small wave age  $c/u_* \sim O(1.5)$  the complete normalized velocity profile resembles wind profiles observed in canopies (e.g., Kaimal and Finnigan 1994, p. 68). Notice that at a fixed  $\zeta$  the wind profile smoothly shifts to the left as the wave surface transitions from ripples to incipient breaking to active breaking, that is, as the underlying surface becomes progressively rougher. This increase in surface roughness correlates well with the steady increase in flow separation and form drag shown in Fig. 5. A log-linear velocity profile begins near  $\zeta \sim (0.06, 0.1)$  for the incipient and active breaker simulations. Then we are able to estimate a bulk roughness  $z_{o,m}$  for our steep waves using the velocity profiles. Choosing  $z_{o,m}$  to match the log-linear relation  $\langle u \rangle / u_* = (1/\kappa) \ln(\zeta/z_{o,m})$  yields  $z_{o,m}/\lambda \approx (1.6, 4.9) \times 10^{-3}$  for incipient and active breaker wave fields; we use a von Kármán constant  $\kappa = 0.41$ . Thus, the incipient and active breakers are approximately 3.7 and 11.9 times rougher than wind ripples alone.

It is illuminating to dissect the momentum balance over resolved breakers given by (5a). Figure 12 shows the ensemble average of the contributions to the momentum balance, namely, the resolved and SGS turbulent fluxes, the pressure–wave slope flux, and their sum

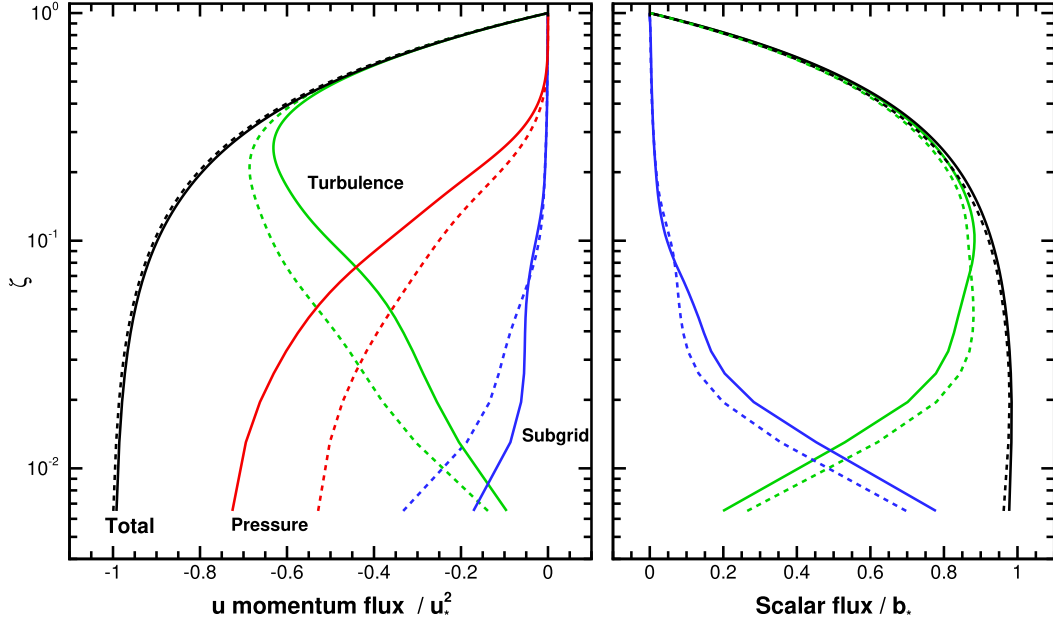


FIG. 12. Vertical profiles of the terms in the (left) ensemble average streamwise momentum and (right) scalar budgets computed in LES wave-following coordinates. Flow over incipient and active breakers is indicated by dashed and solid lines, respectively. The contributions to the streamwise momentum flux are pressure–wave slope correlation (form drag)  $p'_x J$  (red), vertical turbulent momentum flux  $u(W - z_t)$  (green), and the subgrid-scale flux (blue). Contributions to the average scalar flux are vertical turbulent scalar flux  $b(W - z_t)$  (green) and the subgrid-scale flux (blue). In each panel, the total flux is shown in black.

for incipient and active breakers. In wave-following coordinates the total flux is nearly constant for  $\zeta \leq 0.08$ . Above this height the total flux is dominated by the resolved turbulent momentum flux  $\langle u(W - z_t) \rangle$ , which monotonically decreases toward zero at the top of the domain. Below  $\zeta \sim 0.08$ ,  $\langle u(W - z_t) \rangle$  smoothly decreases toward zero at the water surface. No flow through the water surface imposes  $(W - z_t) = 0$ , and hence the pressure and SGS pieces balance the total drag  $u_*^2$ . Notice that the SGS contribution is small near the surface, which is expected given the results in Fig. 5.

#### d. Scalar profiles and budgets

Scalar transport from a wavy water surface is important for a variety of applications (e.g., Emanuel 1999; Wanninkhof et al. 2009; Fairall et al. 2003) but is absent in the majority of laboratory experiments and numerical simulations. Recent studies utilizing DNS and LES that include dynamically active or passive scalars in turbulent flow over resolved waves are Sullivan and McWilliams (2002), Sullivan et al. (2014a), Druzhinin et al. (2016), and Yang and Shen (2017). In these investigations, the wave slope of the wave trains is in an intermediate regime varying from  $0.1 < ak < 0.25$ , and flow separation is not expected. The impact of steep waves with flow separation on the statistics of passive scalar transport in the wave boundary layer is shown

in Figs. 11 and 12 (right panels). An important feature is displayed in Fig. 11; notice at fixed  $\zeta$  the mean scalar profile smoothly shifts to the right as the flow transitions from ripples to incipient breaking to active breaking, that is, in the direction opposite compared to the wind profiles. In other words, the underlying surface appears smoother for scalar concentration in the presence of steep waves. In the log-linear scalar profile  $\langle b_s - b \rangle u_* / b_* = (1/\kappa) \ln(\zeta / z_{o,b})$ , where  $(b_s, b_*)$  are surface values of the scalar concentration and scalar flux; the scalar roughness length for incipient and active breakers is  $z_{o,b} / \lambda = (2.8, 1.1) \times 10^{-4}$ . Thus,  $z_{o,b}$  is smaller than the imposed  $z_{o,s}$ .

If we interpret our results in terms of simple bulk aerodynamic formulas for the fluxes of momentum  $u_*^2 = C_d \langle u \rangle \langle u \rangle$  and scalar  $b_* / u_* = C_b \langle u \rangle \langle b_s - b \rangle$ , the exchange coefficients ( $C_d, C_b$ ) are related to the roughness by

$$\frac{C_d}{C_b} = \frac{\ln(\zeta / z_{o,b})}{\ln(\zeta / z_{o,m})}, \quad (13)$$

using the log-linear profiles for velocity and scalar. Thus, for steep waves the ratio  $C_d / C_b > 1$  for any  $\zeta$ , and the ratio increases with increasing wave slope based on the estimates of surface roughness.

The finding that  $z_{o,m} \geq z_{o,b}$  is further evidence that the classic Reynolds analogy between momentum and



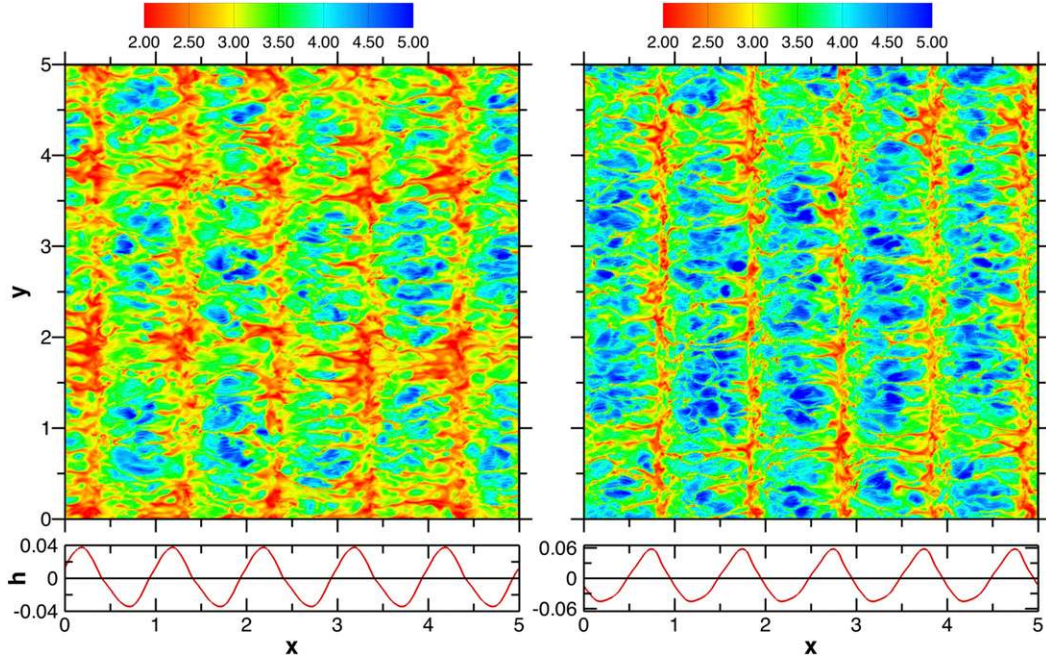


FIG. 13. Visualization of scalar concentration difference  $\Delta b \times 100$  in an  $x$ - $y$  plane near the water surface;  $\Delta b = (b_s - b)/b_s$  with  $b_s = 1$  at the water surface. Turbulent flows with (left) incipient and (right) active breakers. For reference, the wave height  $h(x, t)$  for each flow is shown at the bottom of the panels. Note high (low) scalar concentrations correspond to red (blue) values of  $\Delta b$ .

scalar transport does not hold over a rough surface, including steep waves with flow separation; for further discussion see [Cebeci and Bradshaw \(1988, p. 168\)](#) and [Garratt \(1992, section 4.2\)](#). This somewhat surprising result is explained by comparing the vertical momentum and scalar flux budgets given in [Figs. 12 and 5a and 5b](#). Over a rough surface the pressure drag accounts for the bulk of momentum transport while no such term exists in the scalar flux budget, as shown in [Fig. 12](#). Thus, over steep waves with flow separation, momentum transport is more efficient because of form drag (i.e., pressure fluctuations) compared to inefficient scalar transport by viscous diffusion, consequently  $z_{o,m} > z_{o,b}$ . Physically, in the separated flow regions the scalar transport from the wave surface is inefficient because of weak recirculating surface winds. [Figure 13](#) shows the instantaneous scalar transport  $\Delta b$  is well correlated with the underlying surface wave field:  $\Delta b = (b_s - b)/b_s$ , where  $b$  is the scalar at the first model level. Here,  $\Delta b \gg 0$  indicates that  $b \ll b_s$ , which occurs in the separated flow regions. Meanwhile near the wave crests the surface winds are larger and then  $\Delta b$  becomes smaller, that is,  $b \rightarrow b_s$ . Note the simulations do not include spray generation by breaking waves, which can alter momentum transport and induce significant aerosol production in the marine atmospheric boundary layer, for example, [Richter and Sullivan \(2013\)](#) and [Hwang et al. \(2016\)](#).

## 5. Results for steep unsteady waves

Under strong wind forcing the time evolution of a typical unsteady wave packet (see [Fig. 14](#)) is relatively rapid compared to the turbulence, for example, in our calculations the packet period is  $t \sim 3.27$  for wave age  $c/u_* = 1$ . The short packet life cycle is a consequence of the packet's composition of multiple fast-moving wave modes. Over the packet life cycle, the maximum (most negative) wave slope spans a wide range, rising from 0.1 to a maximum 0.35 and then falling back to 0.1 and less, as shown below in [Fig. 18](#). Note the wave slope exceeds the maximum value for the incipient breaker over the bulk of the packet life cycle, that is,  $-\partial h/\partial x \geq 0.25$  for  $t = [1, 2.5]$ . And the maximum wave slope 0.35 is below the breaking onset in WSIM. Does this unsteady wave height and wave slope variation in the wave packet leave an imprint on the overlying winds? [Figure 18](#) is an important result from the unsteady wave simulations. Here, we show the evolution of the surface form drag and maximum wave slope  $-\partial h/\partial x$  for varying time. The form drag at each time step is first computed from the horizontal average  $\langle p\partial h/\partial x \rangle$  and then the results are normalized by the form drag at an early time  $t = 0.5$ . Essentially, this normalization accounts for the smaller area occupied by the wave packet, that is, on average  $h(\mathbf{x}, t) \neq 0$  over 55% of the LES horizontal domain (see [Fig. 14](#)). First, an excellent correlation between

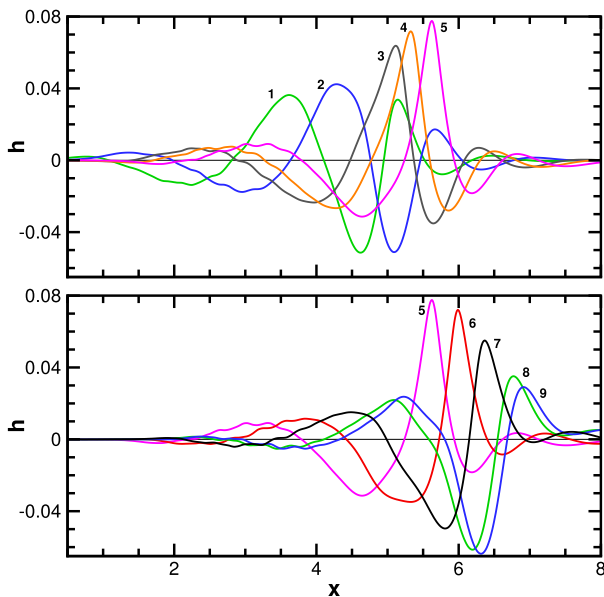


FIG. 14. Time and space evolution of a chirp wave packet for wave age  $c/u_* = 1$ . The curves labeled 1 through 9 correspond to non-dimensional LES time stamps  $t = (0.53, 0.99, 1.52, 1.71, 1.99, 2.34, 2.69, 3.04, 3.16)$ , respectively. The top panel shows the growth of the packet up to the time of maximum amplitude  $t \sim 2$ , while the bottom panel shows the amplitude decay of the packet.

the wave slope and the form drag is observed that supports our premise that the wave slope is the critical variable determining the surface drag. The results also show that the form drag response to varying changes in the packet is quick as the form drag closely tracks the wave slope with minimal time delay. Recall with steady wave trains pressure fluctuations are efficient at transferring momentum to a wavy surface.

In all simulations the waves are strongly forced with similar wave age  $c/u_* \sim 1$ , and then it is interesting to attempt a comparison of the form drag over unsteady and steady cases. We then define a space-time average for the unsteady packet; the spatial average is over the  $x$ - $y$  domain where  $h(\mathbf{x}, t) \neq 0$  followed by a time average over the packet life cycle  $t = [0.5, 3.27]$ . Applying this averaging operator to the wave packet yields an rms wave slope 0.084 and form drag fraction 0.35 (see Fig. 6). The key result is that the form drag of the unsteady packet is 2.4 times larger than the value from a similarly forced uniform monochromatic wave train with rms wave slope  $ak = 0.071$ . Numerical experiments also show that the unsteady wave impact on form drag is only slightly diminished at larger wave age  $c/u_* = 5$ , as shown in Fig. 6. In other words, in the present example an unsteady wave field adds a significant increment to the surface drag and hence unsteadiness to the wind stress, compared to a steady wave field of comparable wave slope.

It is illuminating to interrogate the instantaneous flow fields during the packet evolution to uncover the source of the enhanced form drag and in particular to look for signatures of airflow separation. Streamlines overlaying contours of streamwise velocity and contours of pressure fluctuations in  $x$ - $z$  planes at  $t = (0.93, 1.99, 3.05)$  are displayed in Figs. 15, 16, and 17, respectively. The corresponding maximum wave slope for each time stamp is  $(0.225, 0.327, 0.15)$ . In plotting the results, the range of the  $x$  axis shifts to larger values with increasing time to capture the spatial movement of the packet. For comparison with the steady cases, see Figs. 3 and 4. At  $t = (0.93, 1.99)$ , the velocity and pressure patterns are similar to those found previously over steep steady waves and are suggestive of flow separation. In the example at  $t = 0.93$ , the streamlines leave the wave surface near  $x \sim 4.95$  under a developing coherent vortex that leads to low pressure slightly upstream of the wave trough. In the outer region, the separating streamlines near the wave crest appear to reattach on the windward face of the downstream wave skipping over the wave trough. These patterns are strikingly similar to those obtained for the steady incipient breaker and are indicators of intermittent flow separation. Apparently, multiple wave modes passing through the packet compress the wave trough and simultaneously steepen the faces of the upstream and downstream waves. As a consequence, a strong adverse pressure gradient  $\partial p / \partial x > 0$  forms across a relatively narrow wave trough, and large positive pressure fluctuations develop on the windward face of the downstream wave, as shown in the lower panel of Fig. 15. This adverse pressure gradient induces flow separation on the upstream wave. In other words, the combined action of multiple transient wave modes in a wave packet can induce airflow separation. At  $t = 1.99$ , the streamline, velocity, and pressure patterns all support the interpretation of flow separation. The streamlines leave the wave surface near the wave crest and an expansive low pressure wake develops forward of the crest that leads to high form drag, all in the absence of wave breaking. At  $t = 3.05$ , the packet has nearly collapsed, the wave slope  $< 0.15$ , and the flow patterns are suggestive of attached flow over the wave crest and trough, thus leading to low form drag. Complex flow separation patterns are also found at large wave age  $c/u_* = 5$  (results not shown).

The evolving wave packet impacts the surface form drag but also leaves an imprint on the overlying turbulent airflow. Figure 19 shows time series of the maximum instantaneous vertical velocity in the domain  $|w|_{\max}$  and the resolved turbulent kinetic energy (TKE)  $\text{TKE} = u_i u_i / 2$  at the height  $\zeta = 0.21$ ; TKE is computed from a horizontal average. Both statistics are well

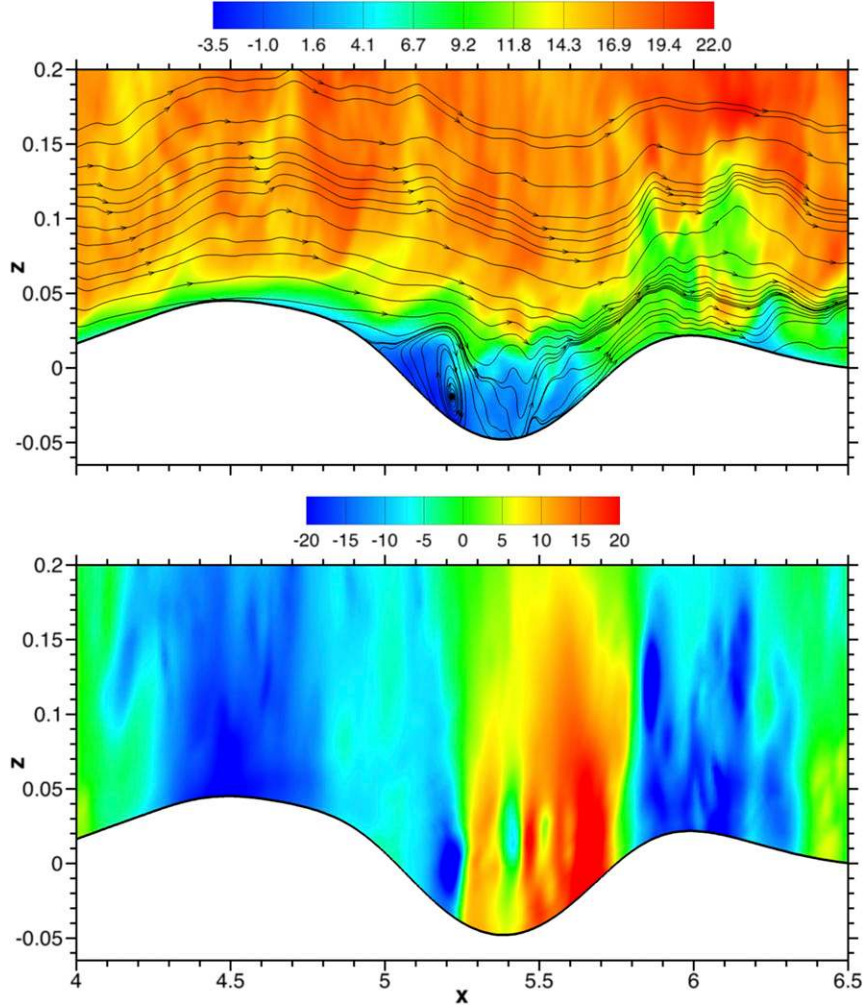


FIG. 15. A snapshot of instantaneous turbulence fields in an  $x$ - $z$  plane for flow over a chirp packet at an early time  $t \sim 0.93$  in Fig. 18. In the top panel, streamlines, generated from the instantaneous vector field  $[u(x, z), w(x, z)]$ , overlay color contours of streamwise velocity  $u$ . The bottom panel shows contours of pressure fluctuations  $p$ . Only a fraction of the horizontal and vertical domains is displayed and the aspect ratio of the plots is not unity. The wind and wave propagation directions are from left to right.

correlated with the growth and decay of the wave packet, but reach maximum values delayed in time compared to the time location where the wave packet amplitude is a maximum. Previously, we found vertical velocity is sensitive to the underlying wave field across a wide range of wave age (e.g., Sullivan et al. 2014a).

In the simulations of turbulent flow over an unsteady wave group the height of the critical level depends on wave age. For wave age  $c/u_* = 5$ ,  $\zeta_c/\lambda = 3.18 \times 10^{-3}$ , which is below the first vertical level in the LES. Similar to the results for steady steep waves, flow visualization shows no clear evidence of a critical layer over the life cycle of the wave packet. We note that we have also

carried out simulations for larger wave age  $c/u_* = 10$  (not shown). Then  $\zeta_c/\lambda \sim 2.35 \times 10^{-2}$ , which is well above the water surface and thus the flow dynamics are resolved by the LES. In this simulation, flow visualization of vertical velocity shows a clear jump across a critical level similar to the results shown in Sullivan et al. (2000, their Fig. 19). However, somewhat surprisingly we find that the presence of a critical level for  $c/u_* = 10$  tends to inhibit flow separation, and hence the form drag over the wave group is lower. In Sullivan et al. (2000, their Fig. 10) the results show that form drag decreases with increasing wave age for  $c/u_* > 10$ . The coupling between flow separation and critical layers is a topic for future work, as suggested by Sajjadi et al. (2014, 2016).



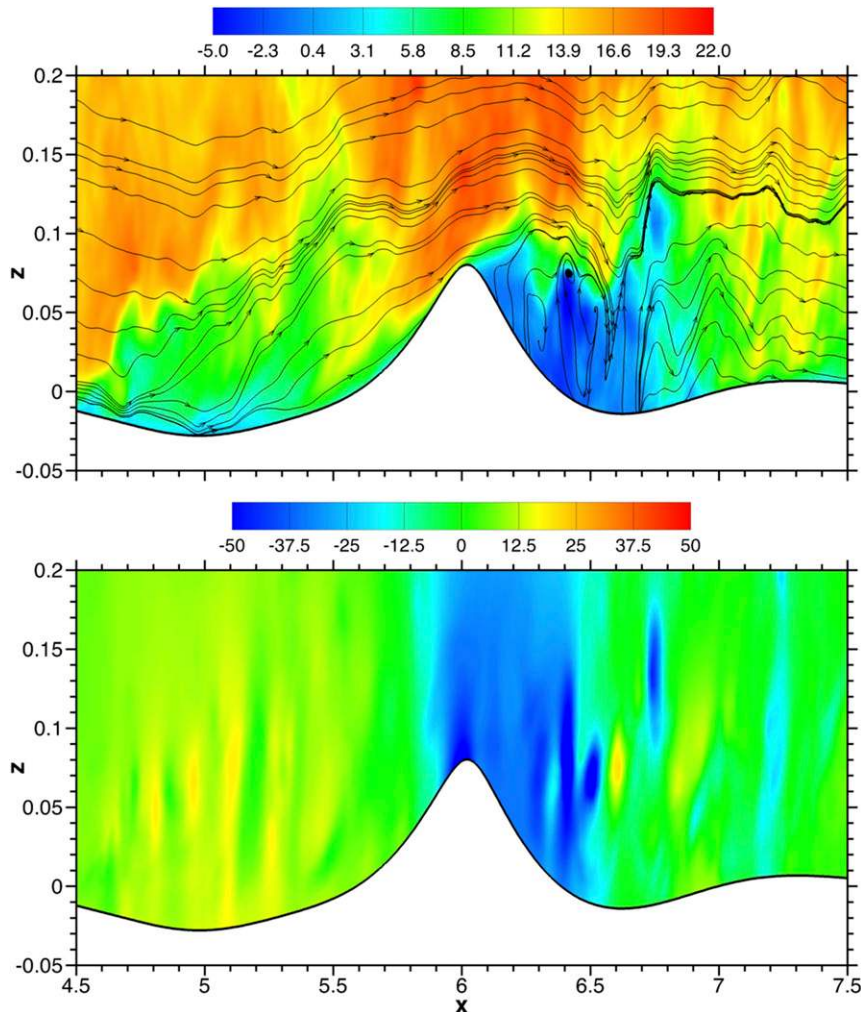


FIG. 16. As in Fig. 15, but near the time of maximum form drag  $t \sim 1.99$  in Fig. 18.

## 6. Summary

High Reynolds number large-eddy simulation (LES; Sullivan et al. 2014a) is used to simulate turbulent flow above very strongly forced steep steady and unsteady wave trains in a wind-wave channel. In the simulations above steady waves, the surface wave height  $h(\mathbf{x}, t)$  is externally imposed based on measurements collected in a wind-wave tank by Banner (1990); thus, the imposed waves are physically realizable and not monochromatic. Two classes of steep breaking waves are investigated: incipient breaking, where the waves are near the onset of breaking, and active breaking with spilling flow down the forward face of the wave. The incipient and active cases are strongly forced with maximum (most negative) wave slope  $-\partial h/\partial x = (0.22, 0.41)$  and wave age  $c/u_* = (1.58, 1.23)$ , respectively;  $c$  is the characteristic wave phase speed, and  $u_*$  is the friction velocity. A simple passive scalar is also added to

the LES model to investigate scalar transport, but spray and bubbles are not considered. In the LES above unsteady waves, the imposed wave field is a temporally and spatially evolving chirp wave packet, or wave group, built using the numerical wave tank code WSIM (Banner et al. 2014). The analysis of the LES focuses on airflow separation and its impacts on surface drag. An ensemble model for the mean wind and scalar, in wave-following coordinates, is developed from the LES equations.

The major findings from the study are as follows:

- In the simulations above steep steady waves, airflow separation is observed for both incipient and active breaking cases. Thus, the LES results support the observations of Veron et al. (2007), Reul et al. (2008), and Buckley and Veron (2016). Separation is highly intermittent, both temporally and spatially, even though the imposed waves are 2D and propagate steadily in time. Based on our results from the incipient case,



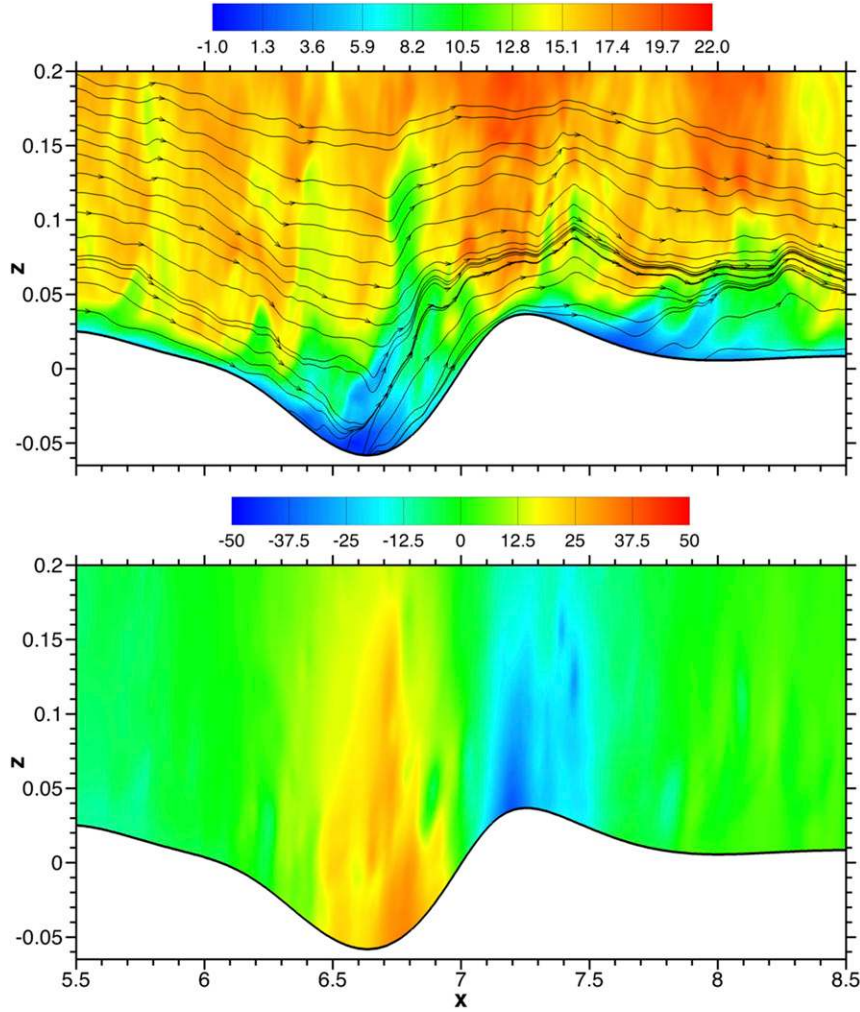


FIG. 17. As in Fig. 15, but at late time  $t \sim 3.05$  in Fig. 18.

intermittent airflow separation occurs prior to the onset of breaking. Thus, the criterion linking separation to wave breaking proposed by Banner and Melville (1976) that is based on flow over solid boundaries is too restrictive. This is also highlighted in more recent studies of separation with unsteady boundaries by Miron and Vétel (2015). However, our study confirms that airflow separation does occur when breaking is operative.

- The partitioning of the surface drag changes markedly between the incipient and active cases. Form (pressure) drag is 54% and 74% of the total stress for the incipient and active cases, respectively. The LES estimates of the form drag are in good agreement with the results reported by Peirson and García (2008). Examination of the pressure-wave slope correlation  $p\partial h/\partial x$  in  $x$ - $y$  planes shows that the correlation is episodic with localized values exceeding 5 times the average wind stress  $u_*^2$ . Because of airflow separation dynamics, a large fraction of the pressure drag is induced at stagnation (or splat) points where the separating flow from a wave crest reattaches on the windward face of a downstream wave, that is, where positive pressure fluctuations are well correlated with positive wave slope.
- Parameter variations varying the wave slope and surface drift of the incipient breaker indicate the root-mean-square (rms) wave slope is the key parameter influencing the pressure drag. Artificially increasing the rms wave slope of the incipient breaker to match that of the active breaker yields nearly the same form drag. Increasing the surface drift had only a minor impact on the form stress levels.
- The nondimensional LES wind profiles  $\langle u \rangle / u_*$  are in very good agreement with the measurements of Banner (1990). A slight sensitivity to the horizontal grid mesh is found. Apparently, fine horizontal resolution  $\Delta x \leq 0.01\lambda$ , where  $\lambda$  is the wavelength, is required to capture the separation and reattachment locations.

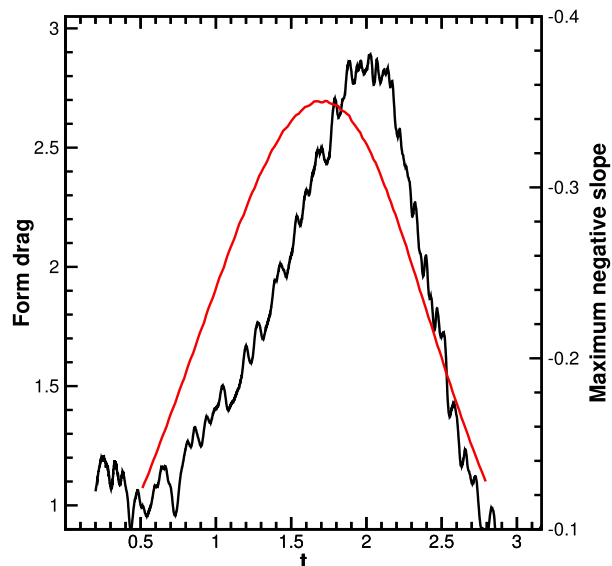


FIG. 18. Time evolution of the maximum (most negative) wave slope  $\partial h/\partial x$  (red; vertical axis on right) and normalized form drag (black; vertical axis on left) for turbulent over the chirp wave packet. The form drag is normalized by its value at  $t \sim 0.5$ .

- The LES wind and scalar profiles both display a logarithmic range above the wave surface. The momentum roughness  $z_{o,m}$  deduced from the wind profiles smoothly increases as the water surface changes from wind ripples to incipient breaking to active breaking. With active breaking the bulk roughness is more than 10 times larger than the roughness from wind ripples. In contrast, the passive scalar roughness  $z_{o,b}$  decreases as the wave surface becomes rougher. This highlights the major differences in momentum and scalar transport over a rough surface. Momentum transport is efficiently carried out by pressure fluctuations, while scalar transport from viscous diffusion is relatively inefficient. These differences are exposed by examining the momentum and scalar flux budgets in wave-following coordinates.
- Wave slope and form drag are well correlated for steady and unsteady waves, which supports the premise that wave slope is the critical variable determining the surface drag.
- Airflow separation also occurs in the LES above an unsteady time- and space-evolving wave packet (group). The wave packet is strongly forced with wave ages  $c/u_* = (1, 5)$ , becoming steeper with increasing time and reaching a maximum wave slope equal to 0.35 but does not break. Intermittent separation becomes readily apparent when the local wave slope in the packet exceeds  $-\partial h/\partial x(\mathbf{x}, t) \geq 0.22$ , similar to the steady incipient breaker. Visualization of the flow

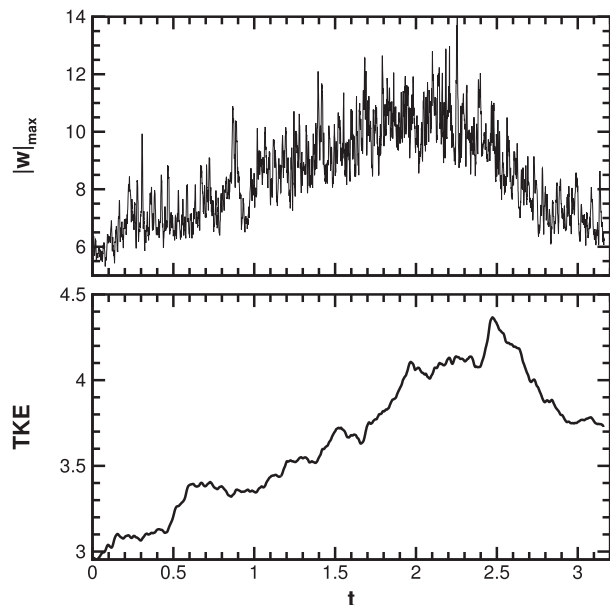


FIG. 19. Time evolution of the (top) maximum vertical velocity  $|w|_{\max}$  in the computational domain and (bottom) average TKE at  $\zeta = \lambda/4$  for turbulent flow over the chirp wave packet.

shows vortical motions in the wave trough and streamlines separating from the wave crest. The change in form drag is rapid and well correlated with the evolving wave slope in the packet. Averaged over the packet life cycle, the rms wave slope is 0.084, but the form drag fraction is nearly 2.4 and 2.1 times larger than a comparably forced monochromatic wave train. As a result, the passage of a transient, strongly forced wave group enhances the form drag and is a potential source of unsteadiness in the wind stress. The present results are particularly relevant to the aerodynamic behavior associated with short wave scales. Our findings likely add further insight into the aerodynamics underpinning the findings of recent ocean studies (Makin et al. 1995; Donelan 1998; Grare et al. 2013a) that short waves support the bulk of the ocean wind stress. For strongly wind-forced oceanic conditions, the wave spectral bandwidth is much broader, and hence its characteristic wave age is larger. Initial LES explorations of turbulent flow over steep waves with increasing wave age hints that the aerodynamics begins a transition from separation-dominated flow to attached flow with emerging critical layer dynamics. Thus, further investigation with numerical simulations and observational studies is needed to map out wind-wave coupling dynamics for steep waves over a range of wave age.

*Acknowledgments.* This work was supported by the Office of Naval Research through the Physical Oceanography

Program. PPS was supported by award N00014-13-G-0223-0002 and the National Science Foundation through the National Center for Atmospheric Research (NCAR). MLB, RPM, and WLP acknowledge support from award N00014-12-10184. This research benefited greatly from computer resources provided by the NCAR Strategic Capability program managed by the NCAR Computational Information Systems Laboratory (<http://n2t.net/ark:/85065/d7wd3xhc>) and the Department of Defense High Performance Computing Modernization Program. We thank the reviewers for their constructive comments that improved the work.

## APPENDIX

### Computation of Unsteady Wave Packet

In the present study we build a 2D chirp packet using the boundary element numerical wave tank code WSIM, a 3D extension of the 2D code developed by Grilli et al. (1989) that solves the single-phase wave motions

for a perfect fluid. It has been applied extensively to the solution of finite-amplitude wave propagation and wave breaking problems. The perfect fluid assumption makes WSIM unable to simulate breaking impact subsequent to surface reconnection. However, its potential theory formulation enables it to simulate wave propagation without numerical viscous diffusion, and thus the simulation of wave generation and development of the onset of breaking events is carried out with great precision. WSIM has been validated extensively for wave evolution in deep and intermediate depth water and shows excellent energy conservation (e.g., Grilli et al. 2001). Its kinematical accuracy has also been validated against the analytical solutions for infinitesimal sine waves in Phillips (1977).

In a numerical wave tank, wave groups over flat bottom topography are generated using a bottom-hinged, flap-type snake wavemaker at one end of the tank. The motion  $X_p(\tilde{t}, y)$  of the wavemaker flap at the lateral location  $y$  followed the class 3 chirp packet motion from Song and Banner (2002):

$$X_p(\tilde{t}, y) = -0.25A_p \left[ 1 + \tanh\left(\frac{4\omega_p \tilde{t}}{N\pi}\right) \right] \left\{ 1 - \tanh\left[\frac{4(\omega_p \tilde{t} - 2N\pi)}{N\pi}\right] \right\} \sin\left[\omega_p \left(\tilde{t} - \frac{\omega_p C_{ch} \tilde{t}^2}{2}\right) + \Phi(y, X_{conv}, Y_{conv})\right], \quad (A1)$$

where  $\tilde{t}$  is the time;  $A_p$  is the amplitude of the paddle motion;  $N$  is the number of waves in the temporal wave packet;  $\omega_p$  is the baseline driving frequency of the paddle, with corresponding linear wavenumber  $k_p$ ; and  $C_{ch} = 1.0112 \times 10^{-2}$  specifies the chirp rate used in this study. The phase  $\Phi(y, X_{conv}, Y_{conv})$  specifies the coordinates of the point of linear convergence (see Dalrymple and Kirby 1988; Dalrymple 1989):

$$\Phi(y, X_{conv}, Y_{conv}) = k_p y \sin\theta(y) + k_p [X_{conv} \cos\theta(y) + Y_{conv} \sin\theta(y)], \quad \text{and} \quad (A2)$$

$$\theta(y, X_{conv}, Y_{conv}) = \arctan\left(\frac{y - Y_{conv}}{X_{conv}}\right), \quad (A3)$$

where  $\theta$  is the focal angle at location  $y$  along the paddle. The downstream boundary opposite the wave paddle is a fully absorbing boundary condition, as in Grilli and Horrillo (1997; also see chapter 3 of Grilli et al. 2010). WSIM uses a boundary element method (BEM) to compute field variables as described by Fochesato and Diaz (2006) and Fochesato et al. (2007). The 16-node quadrilateral elements provide global third-order precision, and high-order tangential derivatives needed for the time discretization are computed

in a local 25-node quadrilateral element curvilinear coordinate system giving fourth-order precision. A fast multipole algorithm is used to invert the BEM problem.

## REFERENCES

- Banner, M. L., 1990: The influence of wave breaking on the surface pressure distribution in wind-wave interaction. *J. Fluid Mech.*, **211**, 463–495, <https://doi.org/10.1017/S0022112090001653>.
- , and W. K. Melville, 1976: On the separation of airflow over water waves. *J. Fluid Mech.*, **77**, 825–842, <https://doi.org/10.1017/S0022112076002905>.
- , and E. H. Fooks, 1985: On the microwave reflectivity of small-scale breaking water waves. *Proc. Roy. Soc. London*, **A399**, 93–109, <https://doi.org/10.1098/rspa.1985.0049>.
- , and W. L. Peirson, 1998: Tangential stress beneath wind-driven air–water interfaces. *J. Fluid Mech.*, **364**, 115–145, <https://doi.org/10.1017/S0022112098001128>.
- , X. Barthelemy, F. Fedele, M. Allis, A. Benetazzo, F. Dias, and W. Peirson, 2014: Linking reduced breaking crest speeds to unsteady nonlinear water wave group behavior. *Phys. Rev. Lett.*, **112**, 114502, <https://doi.org/10.1103/PhysRevLett.112.114502>.
- Belcher, S. E., and J. C. R. Hunt, 1998: Turbulent flow over hills and waves. *Annu. Rev. Fluid Mech.*, **30**, 507–538, <https://doi.org/10.1146/annurev.fluid.30.1.507>.

- Black, P., and Coauthors, 2007: Air-sea exchange in hurricanes: Synthesis of observations from the Coupled Boundary Layers Air-Sea Transfer experiment. *Bull. Amer. Meteor. Soc.*, **88**, 357–374, <https://doi.org/10.1175/BAMS-88-3-357>.
- Buckley, M., 2015: Structure of the airflow above surface waves. Ph.D. thesis, University of Delaware, 154 pp.
- , and F. Veron, 2016: Structure of the airflow above surface waves. *J. Phys. Oceanogr.*, **46**, 1377–1397, <https://doi.org/10.1175/JPO-D-15-0135.1>.
- Catmull, E., and R. Rom, 1974: A class of local interpolating splines. *Computer Aided Geometric Design*, R. E. Barnhill and R. F. Reisenfeld, Eds., Academic Press, 317–326.
- Cebeci, T., and P. Bradshaw, 1988: *Physical and Computational Aspects of Convective Heat Transfer*. Springer-Verlag, 487 pp.
- Dalrymple, R. A., 1989: Directional wavemaker theory with sidewall reflection. *J. Hydraul. Res.*, **27**, 23–34, <https://doi.org/10.1080/00221688909499241>.
- , and J. T. Kirby, 1988: Models for very wide-angle water waves and wave diffraction. *J. Fluid Mech.*, **192**, 33–50, <https://doi.org/10.1017/S0022112088001776>.
- Deardorff, J. W., 1972: Three-dimensional numerical modeling of the planetary boundary layer. *Workshop on Micrometeorology*, D. A. Haugen, Ed., Amer. Meteor. Soc., 271–311.
- Donelan, M. A., 1998: Air-water exchange processes. *Physical Processes in Lakes and Oceans*, J. Imberger, Ed., Coastal and Estuarine Studies, Vol. 54, Amer. Geophys. Union, 19–36.
- , B. K. Haus, N. Reul, W. J. Plant, M. Stiassnie, H. C. Graber, O. B. Brown, and E. S. Saltzman, 2004: On the limiting aerodynamic roughness of the ocean in very strong winds. *Geophys. Res. Lett.*, **31**, L18306, <https://doi.org/10.1029/2004GL019460>.
- Drullion, F., and S. G. Sajjadi, 2016: Growth of groups of wind generated waves. *Proc. IMA Conf. on Turbulence, Waves and Mixing*, Cambridge, United Kingdom, Institute of Mathematics and its Applications, 128–131.
- Druzhinin, O., Y. Troitskaya, and S. Zilitinkevich, 2016: Stably stratified turbulence over a wavy water surface. Part 1: Stationary turbulence regime. *Quart. J. Roy. Meteor. Soc.*, **142**, 759–772, <https://doi.org/10.1002/qj.2677>.
- Emanuel, K. A., 1999: Thermodynamic control of hurricane intensity. *Nature*, **401**, 665–669, <https://doi.org/10.1038/44326>.
- Fairall, C. W., E. F. Bradley, J. E. Hare, A. A. Grachev, and J. B. Edson, 2003: Bulk parameterization of air-sea fluxes: Updates and verification for the COARE algorithm. *J. Climate*, **16**, 571–591, [https://doi.org/10.1175/1520-0442\(2003\)016<0571:BPOASF>2.0.CO;2](https://doi.org/10.1175/1520-0442(2003)016<0571:BPOASF>2.0.CO;2).
- Fochesato, C., and F. Diaz, 2006: A fast method for nonlinear three-dimensional free-surface waves. *Proc. Roy. Soc. London*, **A462**, 2715–2735, <https://doi.org/10.1098/rspa.2006.1706>.
- , S. Grilli, and F. Diaz, 2007: Numerical modeling of extreme rogue waves generated by directional spreading. *Wave Motion*, **44**, 395–416, <https://doi.org/10.1016/j.wavemoti.2007.01.003>.
- Garratt, J. R., 1992: *The Atmospheric Boundary Layer*. Cambridge University Press, 316 pp.
- Gent, P. R., and P. A. Taylor, 1977: A note on ‘separation’ over short wind waves. *Bound.-Layer Meteor.*, **11**, 65–87, <https://doi.org/10.1007/BF00221825>.
- Gong, W., P. A. Taylor, and A. Dörnbrack, 1996: Turbulent boundary-layer flow over fixed aerodynamically rough two-dimensional sinusoidal waves. *J. Fluid Mech.*, **312**, 1–37, <https://doi.org/10.1017/S0022112096001905>.
- Grare, L., L. Lenain, and W. Melville, 2013a: Wave-coherent air-flow and critical layers over ocean waves. *J. Phys. Oceanogr.*, **43**, 2156–2172, <https://doi.org/10.1175/JPO-D-13-056.1>.
- , W. L. Peirson, H. Branger, J. W. Walker, J.-P. Giovanangeli, and V. Makin, 2013b: Growth and dissipation of wind-forced deep-water waves. *J. Fluid Mech.*, **722**, 5–50, <https://doi.org/10.1017/jfm.2013.88>.
- Grilli, S. T., and J. Horrillo, 1997: Numerical generation and absorption of fully nonlinear periodic waves. *J. Eng. Mech.*, **123**, 1060–1069, [https://doi.org/10.1061/\(ASCE\)0733-9399\(1997\)123:10\(1060\)](https://doi.org/10.1061/(ASCE)0733-9399(1997)123:10(1060)).
- , J. Skourup, and I. A. Svendsen, 1989: An efficient boundary element method for nonlinear water waves. *Eng. Anal. Bound. Elem.*, **6**, 97–107, [https://doi.org/10.1016/0955-7997\(89\)90005-2](https://doi.org/10.1016/0955-7997(89)90005-2).
- , P. Guyenne, and F. Dias, 2001: A fully nonlinear model for three-dimensional overturning waves over arbitrary bottom. *Int. J. Numer. Methods Fluids*, **35**, 829–867, [https://doi.org/10.1002/1097-0363\(20010415\)35:7<829::AID-FLD115>3.0.CO;2-2](https://doi.org/10.1002/1097-0363(20010415)35:7<829::AID-FLD115>3.0.CO;2-2).
- , F. Dias, P. Guyenne, C. Fochesato, and F. Enet, 2010: Progress in fully nonlinear potential flow modeling of 3D extreme ocean waves. *Advances in Numerical Simulation of Nonlinear Water Waves*, Q. Ma, Ed., Advances in Coastal and Ocean Engineering, Vol. 11, World Scientific, 75–128, [https://doi.org/10.1142/9789812836502\\_0003](https://doi.org/10.1142/9789812836502_0003).
- Grue, J., L. Romero, J. Kleiss, and W. K. Melville, 2008: Orbital velocity in spatial ocean wave elevation measurement: Non-linear computation and approximation. *27th Int. Conf. on Offshore Mechanics and Arctic Engineering*, Estoril, Portugal, American Society of Mechanical Engineers, 135–141, <https://doi.org/10.1115/OMAE2008-57205>.
- Hara, T., and P. P. Sullivan, 2015: Wave boundary layer turbulence over surface waves in a strongly forced condition. *J. Phys. Oceanogr.*, **45**, 868–883, <https://doi.org/10.1175/JPO-D-14-0116.1>.
- Henn, D. S., and R. I. Sykes, 1999: Large-eddy simulations of flow over wavy surfaces. *J. Fluid Mech.*, **383**, 75–112, <https://doi.org/10.1017/S0022112098003723>.
- Hristov, T., S. D. Miller, and C. Friehe, 2003: Dynamical coupling of wind and ocean waves through wave-induced air flow. *Nature*, **422**, 55–58, <https://doi.org/10.1038/nature01382>.
- Hwang, P. A., I. B. Savelyev, and M. D. Angelova, 2016: Breaking waves and near-surface sea spray aerosol dependence on changing winds: Wave breaking efficiency and bubble-related air-sea interaction processes. *IOP Conf. Ser.: Earth Environ. Sci.*, **35**, 012004, <https://doi.org/10.1088/1755-1315/35/1/012004>.
- Janssen, P. A. E. M., 2008: Progress in ocean wave forecasting. *J. Comput. Phys.*, **227**, 3572–3594, <https://doi.org/10.1016/j.jcp.2007.04.029>.
- Kaimal, J. C., and J. J. Finnigan, 1994: *Atmospheric Boundary Layer Flows: Their Structure and Measurement*. Oxford University Press, 289 pp.
- Li, P. Y., D. Xu, and P. A. Taylor, 2000: Numerical modelling of turbulent airflow over water waves. *Bound.-Layer Meteor.*, **95**, 397–425, <https://doi.org/10.1023/A:1002677312259>.
- Longuet-Higgins, M. S., 1984: Statistical properties of wave groups in a random sea state. *Proc. Roy. Soc. London*, **A312**, 219–250, <https://doi.org/10.1098/rsta.1984.0061>.
- Makin, V. K., V. N. Kudryavtsev, and C. Mastenbroek, 1995: Drag of the sea surface. *Bound.-Layer Meteor.*, **73**, 159–182, <https://doi.org/10.1007/BF00708935>.
- McWilliams, J. C., C.-H. Moeng, and P. P. Sullivan, 1999: Turbulent fluxes and coherent structures in marine boundary layers: Investigations by large-eddy simulation. *Air-Sea Exchange: Physics, Chemistry, Dynamics, and Statistics*, G. Geernaert, Ed., Kluwer, 507–538.
- Melville, W. K., M. R. Loewen, F. C. Felizardo, A. T. Jessup, and M. J. Buckingham, 1988: Acoustic and microwave signatures of breaking waves. *Nature*, **336**, 54–56, <https://doi.org/10.1038/336054a0>.



- Miron, P., and J. Vétel, 2015: Towards the detection of moving separation in unsteady flows. *J. Fluid Mech.*, **779**, 819–841, <https://doi.org/10.1017/jfm.2015.461>.
- Mironov, D. V., and P. P. Sullivan, 2016: Second-moment budgets and mixing intensity in the stably stratified atmospheric boundary layer over thermally heterogeneous surfaces. *J. Atmos. Sci.*, **73**, 449–464, <https://doi.org/10.1175/JAS-D-15-0075.1>.
- Moeng, C.-H., 1984: A large-eddy-simulation model for the study of planetary boundary-layer turbulence. *J. Atmos. Sci.*, **41**, 2052–2062, [https://doi.org/10.1175/1520-0469\(1984\)041<2052:ALESMF>2.0.CO;2](https://doi.org/10.1175/1520-0469(1984)041<2052:ALESMF>2.0.CO;2).
- , and J. C. Wyngaard, 1989: Evaluation of turbulent transport and dissipation closures in second-order modeling. *J. Atmos. Sci.*, **46**, 2311–2330, [https://doi.org/10.1175/1520-0469\(1989\)046<2311:EOTTAD>2.0.CO;2](https://doi.org/10.1175/1520-0469(1989)046<2311:EOTTAD>2.0.CO;2).
- , and P. P. Sullivan, 2015: Large-eddy simulation. *Encyclopedia of Atmospheric Sciences*, 2nd ed. G. R. North, F. Zhang, and J. Pyle, Eds., Vol. 4, Academic Press, 232–240.
- Pearson, W. L., and A. W. Garcia, 2008: On the wind-induced growth of slow water waves of finite steepness. *J. Fluid Mech.*, **608**, 243–274, <https://doi.org/10.1017/S002211200800205X>.
- , J. W. Walker, and M. L. Banner, 2014: On the microphysical behaviour of wind-forced water surfaces and consequent re-aeration. *J. Fluid Mech.*, **743**, 399–447, <https://doi.org/10.1017/jfm.2013.681>.
- Perlin, M., W. Choi, and Z. Tian, 2013: Breaking waves in deep and intermediate waters. *Annu. Rev. Fluid Mech.*, **45**, 115–145, <https://doi.org/10.1146/annurev-fluid-011212-140721>.
- Phillips, O. M., 1977: *Dynamics of the Upper Ocean*. Cambridge University Press, 336 pp.
- Reul, N., H. Branger, and J.-P. Giovanangeli, 2008: Air flow structure over short-gravity breaking waves. *Bound.-Layer Meteor.*, **126**, 477–505, <https://doi.org/10.1007/s10546-007-9240-3>.
- Richter, D. H., and P. P. Sullivan, 2013: Sea surface drag and the role of spray. *Geophys. Res. Lett.*, **40**, 656–660, <https://doi.org/10.1002/grl.50163>.
- Sajjadi, S. G., J. C. R. Hunt, and F. Drullion, 2014: Asymptotic multi-layer analysis of wind over unsteady monochromatic surface waves. *J. Eng. Math.*, **84**, 73–85, <https://doi.org/10.1007/s10665-013-9663-4>.
- , —, and —, 2016: Growth of unsteady wave groups by shear flows. *Proc. IMA Conf. on Turbulence, Waves and Mixing*, Cambridge, United Kingdom, Institute of Mathematics and its Applications, 79–84.
- Song, J. B., and M. L. Banner, 2002: On determining the onset and strength of breaking for deep water waves. Part I: Unforced irrotational wave groups. *J. Phys. Oceanogr.*, **32**, 2541–2558, <https://doi.org/10.1175/1520-0485-32.9.2541>.
- Sullivan, P. P., and J. C. McWilliams, 2002: Turbulent flow over water waves in the presence of stratification. *Phys. Fluids*, **14**, 1182–1195, <https://doi.org/10.1063/1.1447915>.
- , and E. G. Patton, 2011: The effect of mesh resolution on convective boundary-layer statistics and structures generated by large-eddy simulation. *J. Atmos. Sci.*, **68**, 2395–2415, <https://doi.org/10.1175/JAS-D-10-05010.1>.
- , J. C. McWilliams, and C.-H. Moeng, 1994: A subgrid-scale model for large-eddy simulation of planetary boundary-layer flows. *Bound.-Layer Meteor.*, **71**, 247–276, <https://doi.org/10.1007/BF00713741>.
- , —, and —, 1996: A grid nesting method for large-eddy simulation of planetary boundary layer flows. *Bound.-Layer Meteor.*, **80**, 167–202, <https://doi.org/10.1007/BF00119016>.
- , —, and —, 2000: Simulation of turbulent flow over idealized water waves. *J. Fluid Mech.*, **404**, 47–85, <https://doi.org/10.1017/S0022112099006965>.
- , —, and W. K. Melville, 2007: Surface gravity wave effects in the oceanic boundary layer: Large-eddy simulation with vortex force and stochastic breakers. *J. Fluid Mech.*, **593**, 405–452, <https://doi.org/10.1017/S002211200700897X>.
- , —, and E. G. Patton, 2014a: Large-eddy simulation of marine boundary layers above a spectrum of moving waves. *J. Atmos. Sci.*, **71**, 4001–4027, <https://doi.org/10.1175/JAS-D-14-0095.1>.
- , and Coauthors, 2014b: Large-eddy simulations of marine boundary layers above a measured spectrum of phase-resolved nonlinear ocean waves. *21st Symp. on Boundary Layers and Turbulence*, Leeds, United Kingdom, Amer. Meteor. Soc., 9B.1, <https://ams.confex.com/ams/21BLT/webprogram/Paper247537.html>.
- Szuber, D., F. Grossi, A. J. Garcia, Y. Hoarou, J. C. R. Hunt, and M. Braza, 2015: Shock-vortex shear-layer interaction in the transonic flow around a supercritical airfoil at high Reynolds number in buffet conditions. *J. Fluids Struct.*, **55**, 276–302, <https://doi.org/10.1016/j.jfluidstructs.2015.03.005>.
- Thomas, P. D., and C. K. Lombard, 1979: Geometric conservation law and its application to flow computations on moving grids. *AIAA J.*, **17**, 1030–1037, <https://doi.org/10.2514/3.61273>.
- Veron, F., G. Saxena, and S. K. Misra, 2007: Measurements of the viscous tangential stress in the airflow above wind waves. *Geophys. Res. Lett.*, **34**, L19603, <https://doi.org/10.1029/2007GL031242>.
- Wanninkhof, R., W. E. Asher, D. T. Ho, C. S. Sweeney, and W. R. McGillis, 2009: Advances in quantifying air-sea gas exchange and environmental forcing. *Annu. Rev. Mar. Sci.*, **1**, 213–244, <https://doi.org/10.1146/annurev.marine.010908.163742>.
- Wu, J., 1975: Wind-induced drift currents. *J. Fluid Mech.*, **68**, 49–70, <https://doi.org/10.1017/S0022112075000687>.
- Wyngaard, J. C., L. J. Peltier, and S. Khanna, 1998: LES in the surface layer: Surface fluxes, scaling, and SGS modeling. *J. Atmos. Sci.*, **55**, 1733–1754, [https://doi.org/10.1175/1520-0469\(1998\)055<1733:LITSLS>2.0.CO;2](https://doi.org/10.1175/1520-0469(1998)055<1733:LITSLS>2.0.CO;2).
- Yang, D., and L. Shen, 2010: Direct-simulation-based study of turbulent flow over various waving boundaries. *J. Fluid Mech.*, **650**, 131–180, <https://doi.org/10.1017/S0022112009993557>.
- , and —, 2017: Direct numerical simulation of scalar transport in turbulent flows over progressive surface waves. *J. Fluid Mech.*, **819**, 58–103, <https://doi.org/10.1017/jfm.2017.164>.
- Zhou, J., R. J. Adrian, S. Balachandrar, and T. M. Kendall, 1999: Mechanisms for generating coherent packets of hairpin vortices in channel flow. *J. Fluid Mech.*, **387**, 353–396, <https://doi.org/10.1017/S002211209900467X>.